Baghdad Science Journal

Volume 23 | Issue 5 Article 29

5-29-2026

A New Hybrid Approach for Magnetohydrodynamic Flow Over a Stretching Surface With Nanofluid

Ammar Al-Salih
Department of Mathematics, College of Education for Pure Science, Basrah University, Basrah, Iraq, ammar.radhii@uobasrah.edu.iq

Abdul-Sattar Jaber Al-Saif
Department of Mathematics, College of Education for Pure Science, Basrah University, Basrah, Iraq, abdulsattar.ali@uobasrah.edu.iq

How to Cite this Article

Al-Salih, Ammar and Al-Saif, Abdul-Sattar Jaber (2026) "A New Hybrid Approach for Magnetohydrodynamic Flow Over a Stretching Surface With Nanofluid," *Baghdad Science Journal*: Vol. 23: Iss. 5, Article 29.
DOI: https://doi.org/10.21123/2411-7986.5313

BAGHDAD SCIENCE JOURNAL 2026;23(5):1948–1971

RESEARCH ARTICLE

A New Hybrid Approach for Magnetohydrodynamic Flow Over a Stretching Surface With Nanofluid

Ammar Al-Salih *, **Abdul-Sattar Jaber Al-Saif**

Department of Mathematics, College of Education for Pure Science, Basrah University, Basrah, Iraq

ABSTRACT

The current investigation focuses on developing a semi-analytical technique aimed at estimating the solutions of magnetohydrodynamics flow with Casson tri-hybrid nanofluid ($TiO_2 - SiO_2 - Al_2O_3/blood$) flowing over a stretchable surface along two-dimensional space. To solve the obtained nonlinear coupled differential equations in the problem formulation, the proposed semi-analytical approach makes use of the Shehu reduced differential transform Padé method (SRDTPM). Several physical parameters, such as slip effect, porosity, magnetic strength, and Casson number, were considered for examining the effect on momentum, while radiation parameter, heat generation/absorption, temperature-dependent heat sink/source term, and Biot number were analyzed for energy transfer. The results revealed an inverse relation between fluid velocity (both primary and secondary velocities) and porosity/magnetic strength, whereas an increase in the value of the Casson number resulted in higher secondary velocity. Further, it is observed that higher values of the heat sink/source terms and Biot numbers led to an increase in the fluid temperature.

Keywords: Convergence analysis, Padé approximant, Reduced differential transform method, Shehu transform, Tri-hybrid nanofluid

Introduction

The disciplines of fluid dynamics and dynamical systems have always formed an important part of applied mathematics and engineering, providing valuable insights into flow-related processes occurring within diverse domains, such as extensive surfaces and porous media. In recent times, the use of nanotechnology in such studies has received considerable attention because of the benefits it provides in improving thermal and hydrodynamical performance. It should be mentioned that blood is often used as a fundamental fluid for many studies involving fluid dynamics. The flow properties of blood are evaluated using mathematical models, which consider its unique physical and chemical nature. These studies utilize both numerical and analytical methods to obtain accurate and efficient solutions to complicated problems, thereby enhancing the understanding of interactions between physical factors such as viscosity, heat transfer, and the effects of nanomaterials. These methods have enabled the treatment of many innovative dynamic systems and the improvement of biological processes, such as enhancing blood flow in arteries, as well as industrial applications, such as using nanomaterials to improve performance.

In recent years, research has increasingly focused on developing mathematical models and investigating the effect of physical and chemical variables on the dynamic behavior of fluid (blood) flow in different media. For example, Nasresfahani and Eslahchi [1] used a combination of the finite difference method and the collection method to solve the independent boundary problem of an artery plaque growth model. Manchi

Received 18 May 2025; revised 8 October 2025; accepted 15 November 2025.
Available online 29 May 2026

* Corresponding author.
E-mail addresses: ammar.radhii@uobasrah.edu.iq (A. Al-Salih), abdulsattar.ali@uobasrah.edu.iq (A.-S. J. Al-Saif).

https://doi.org/10.21123/2411-7986.5313

and Ponalagusamy [2] utilized the combined Laplace-Hankel transform method to get an analytical solution for temperature distribution in a nanofluid traversing an angled artery with various constrictions. Additionally, they employed the finite difference method to calculate flow velocity numerically. Ali et al. [3] applied the Adams-Bashforth method to analyze the influence of specific heat on magnetohydrodynamic flow of a hybrid nanofluid within a wide cylinder. Asfour and Ibrahim [4] utilized the finite difference method and multi-step differential transform method to derive solutions for a model depicting electro-osmotic blood flow of magnetic Sutterby nanofluid. Bataineh et al. [5] implemented the Bernstein collocation method to derive a solution for the application of magnetohydrodynamics in addressing Jeffery-Hamel blood flow. Jamil et al. [6] relied on Laplace transform and finite Hankel transform techniques to investigate non-Newtonian magnetic blood flow in oblique arteries. Shamshuddin et al. [7] adopted the homotopy analysis approach to get semi-analytical solutions for ordinary differential equations arising from the mathematical description of magnetic hybrid nanofluid flow on a spinning, stretchable disk. Mangamma et al. [8] examined magnetohydrodynamic flow over an asymmetrically moving plate and adopted the Galerkin finite element method to address the model equations. Vaidya et al. [9] implemented a perturbation approach to get solutions for governing equations concerning the flow of viscous nanohybrid fluids within a narrowed artery. Gunisetty et al. [10] used the homotopy perturbation method to explore flow and temperature characteristics of a hybrid electromagnetic-hydrodynamic nanofluid over a rotating porous disk. Sajjan et al. [11] analyzed pulsating hydromagnetic flow of a micropolar ternary hybrid nanofluid with the help of the Runge-Kutta scheme and the shooting method for solving the governing partial differential equations. Oyekunle et al. [12] looked at the hydrodynamic flow of a nanofluid influenced by buoyancy through a porous shrinkage sheet. They applied the collocation method to deal with nonlinear differential equations that govern fluid flow, utilizing Legendre polynomials to approximate unknown functions. Khan [13] applied Laplace and Sumudu transforms to analyze velocity and temperature distributions of a rotating magnetohydrodynamic flow in a tetra-hybrid nanofluid within a porous medium. Agbaje et al. [14] employed the spectral quasilinearization method to examine the influence of a hybrid micropolar nanofluid on blood flow within a parallel channel.

Numerous iterative methods have demonstrated effectiveness in addressing challenges associated with nonlinear flows; however, many of them encounter significant difficulties due to the computational complexity involved. These methods often require substantial time and effort to achieve accurate solutions. Numerical and mathematical methods like the differential quadrature method [15], the differential transform method [16,17] the homotopy perturbation method [18], the collocation method [19], and the optimal homotopy method [20] have been used to study the movement of fluids and blood.

Acknowledging constraints of these techniques, researchers and engineers have progressively used semi-analytical methods to examine fluid and blood flow in various scenarios, including stretched surfaces, porous media, and vascular systems. These methods allow for a deeper comprehension of the dynamics of fluid and blood flow, which in turn allows for the creation of novel approaches to solving difficult problems in biological systems and fluid mechanics. Pavithra et al. [21] investigated the use of a ternary hybrid fluid to drive a longitudinal fin, using Adomian decomposition-Sumudu transform approach to examine heat transmission characteristics within the fin. Arif et al. [22] performed a heat transfer study of a Casson tri-hybrid nanofluid model in blood, employing Laplace and Fourier transforms to resolve governing equations. Al-Griffi and Al-Saif [23] utilized the Yang transform approach in conjunction with the homotopy perturbation method to get analytical approximate solutions for equations that describe pulsatile blood flow in thin tapering arteries. Al-Griffi and Al-Saif [24] integrated the Akbari-Ganji method with the homotopy perturbation method to obtain analytical solutions for blood flow in a slightly stenotic oblique artery. Abdulameer and Al-Saif [25] merged the Fourier transform, Laplace transform, and homotopy perturbation methods to obtain approximate analytical solutions for fluid flow and heat transfer in a horizontal concentric cylindrical ring. Ahsan et al. [26] applied the high-order Haar wavelet collocation method to obtain solutions for systems of nonlinear ordinary differential equations. Abdul-Wahab and Al-Saif [27] utilize Chebyshev series, Akbari-Ganji method, and a modified homotopy perturbation technique to address nonlinear differential equations governing blood flow in narrow arteries. Ahsan et al. [28] employed the collocation method based on Haar wavelets to solve fifth-order linear and nonlinear differential equations.

Most previous research has focused on improving analytical and semi-analytical methods to obtain accurate or approximate solutions for complicated fluid flow models. Recent studies emphasize growing interest in combining these methods to reduce complexity and computational effort compared to using only analytical techniques. This approach helps save both time and resources. Consequently, this study will introduce a novel algorithm founded on three fundamental keys. The first key is the Shehu transform (ST) introduced by Maitama and Zhao,[29] which has been applied to solving complicated problems in scientific and technical fields and is recognized for its precision in resolving ordinary and partial differential equations.[30,31] The second is the reduced differential transform method (RDTM) developed by Keskin and Otranc,[32] which gives analytical approximate solutions with fast convergence and low processing requirements. The third is the Padé approximant, which enhances the accuracy and convergence of approximate solutions obtained from RDTM.[33] The combination of these keys in the proposed Shehu reduced differential transform Padé method (SRDTPM) significantly improves the efficiency of solving differential equations by improving accuracy and convergence. This technique is used to investigate three-dimensional fluid dynamics of a ti-hybrid ($TiO_2 - SiO_2 - Al_2O_3$) Casson nanofluid across a bidirectionally stretched surface. The flow is investigated along the start equation script x- and start equation script y-axes, with the x- and y-axes, with z-axis perpendicular to the surface. Slip effect, porosity, magnetic field, and Casson fluid parameters effects on the momentum equation are studied, as well as radiation effect, temperature effect, and heat generation or absorption effects on the energy equation. From a mathematical aspect, SRDTPM shows relatively better accuracy and convergence compared to RDTM, confirming the effectiveness of the method and its superiority over other methods. The findings show that mixed nanofluids might be able to help heat move more efficiently. These innovations might assist in creating better thermal management systems, which would include heat exchangers in industry. In the healthcare sector, the use of blood as the working fluid and nanoparticles will help enhance the thermal conductivity of biological tissues. This will not only boost the efficiency of hyperthermia therapy for cancers but will also help in delivering medication to target areas accurately.

Materials and methods

The core concept of SRDTPM involves using the Shehu transform, the reduced differential transform method, and Padé approximations to accurately and reliably solve complex fluid flow problems. The process of solving such problems using this method will be discussed further in the following sections:

Shehu transform (ST)

The Shehu transform, which was first presented by Maitama and Zhao in 2019[29] can be viewed as an expansion of the traditional Laplace transform. This mathematical tool has been instrumental in deriving exact analytical solutions for problems in several fields of study. The Shehu transform is especially useful in solving ordinary and partial differential equations. For a function $h(x)$, the Shehu transform, denoted by $\Gamma(s_1, s_2)$, is mathematically defined through the following integral:

$$\mathbb{S}(h(x)) = \int_0^\infty h(x)e^{-\frac{s_1}{s_2}x}\,dx = \lim_{a\to\infty}\int_0^a h(x)e^{-\frac{s_1}{s_2}x}\,dx = \Gamma(s_1, s_2), \tag{1}$$

where, a is denoting a constant, while s_1 and s_2 are positive variables which are related to the Shehu transform. The inverse Shehu transform, which is indicated as $\mathbb{S}^{-1}(\Gamma(s_1, s_2))$, can be defined for $x \geq 0$ as follows:

$$h(x) = \mathbb{S}^{-1}(\Gamma(s_1, s_2)) = \frac{1}{2\pi i}\int_{a-i\infty}^{a+i\infty}\frac{1}{s_2}\Gamma(s_1, s_2)e^{-\frac{s_1}{s_2}x}\,ds_1. \tag{2}$$

The Shehu transform has been successfully coupled with several other semi-analytical methods in order to benefit from their strengths and mitigate the weaknesses of traditional analytical methods.[29,30,34] The resulting strategy has been shown to be highly effective at solving difficult mathematical and engineering problems.

Reduced differential transform method (RDTM)

The reduced differential transform method (RDTM) was proposed by Keskin and Otranc in 200932 and can be seen as an improvement over the classic differential transform method (DTM). RDTM allows finding not only approximate but also exact analytical solutions to many problems related to engineering, physics, and biology. This technique was introduced to avoid computational complications of the conventional DTM.[35] For a function $q(r, s)$ that is continuously differentiable with respect to r and s, the reduced differential transform is defined as follows:

$$Q_i(\mathscr{r}) = \frac{1}{i!}\left[\frac{\partial^i q(\mathscr{r},\mathscr{s})}{\partial \mathscr{s}^i}\right]_{\mathscr{s}=0}, \tag{3}$$

where $Q_i(\mathscr{r})$ is referring to the function after transformation, while $q(\mathscr{r},\mathscr{s})$ is representing the initial, untransformed function. The inverse RDT, which is applied to $Q_i(\mathscr{r})$ can be expressed through the following series expansion:

$$q(\mathscr{r},\mathscr{s}) = \sum_{i=0}^{\infty} Q_i(\mathscr{r})\,\mathscr{s}^i. \tag{4}$$

Appling Eq. (3) in the inverse of the RDT equation will lead to:

$$q(\mathscr{r},\mathscr{s}) = \sum_{i=0}^{\infty} \frac{\mathscr{s}^i}{i!}\,\frac{\partial^i q(\mathscr{r},\mathscr{s})}{\partial \mathscr{s}^i}\bigg|_{\mathscr{s}=0} \tag{5}$$

Padé approximant

Padé Approximant stands out as a very useful method within the realm of mathematics that can be used to enhance accuracy in numerical approximation. Unlike the Taylor series, which involves only polynomial approximation, the Padé approximant represents an equation by a quotient of two polynomials. This approach tends to generate better results because of improved accuracy and stability.[36]

Take in consideration the analytic function $\hat{\mathrm{A}}(x)$ which is represented by its Maclaurin series expansion:

$$\hat{\mathrm{A}}(x) = \sum_{m=0}^{\infty} \hat{\mathrm{s}}_m x^m. \tag{6}$$

The Padé approximant for the function $\hat{\mathrm{A}}(x)$, which can be represented as P_d^n, is defined as the following:

$$P_d^n = \sum_{m=0}^{\infty} \hat{\mathrm{s}}_m x^m = \frac{\hat{\mathrm{N}}(x)}{\hat{\mathrm{D}}(x)} = \frac{\sum_{m=0}^{n} \hat{\mathrm{a}}_m x^m}{1+\sum_{m=1}^{d} \hat{\mathrm{b}}_m x^m}, \tag{7}$$

Such that n and d are denoting the orders of the numerator and denominator, respectively. Using the construction, the Padé approximant goes along with the terms of P_d^n with those in the Taylor series expansion of the function $\hat{\mathrm{A}}(x)$, which results in achieving a highly accurate approximation. From Eq. (7). The following relation can be achieved:

$$\hat{\mathrm{N}}(x) - \hat{\mathrm{D}}(x)\; P_d^n = o\left(x^{n+d+1}\right). \tag{8}$$

This relation leads to a system of linear algebraic equations that can be solved to determine the coefficients of the polynomials. Using symbolic computation software such as Maple, the coefficients $\hat{\mathrm{a}}_m$ $(0 \le m \le n)$ and $\hat{\mathrm{b}}_m$ $(1 \le m \le n)$ can be determined.[37]

To clarify the solution algorithm for SRDTPM, consider a general nonlinear standard differential equation of the form[38]:

$$D\left(y(x)\right) + R\left(y(x)\right) + N\left(y(x)\right) + \delta(x) = 0, \tag{9}$$

where D and R are linear operators, N is a nonlinear operator, and $\delta(x)$ is a defined function.

Description of the SRDTPM algorithm

To illustrate the solution algorithm of SRDTPM, we outline its application steps as follows:

- **Step 1:** Apply the Shehu transform to the Eq. (9) yields the following:

$$\mathbb{S}\left(D\left(y\left(x\right)\right)+R\left(y\left(x\right)\right)+N\left(y\left(x\right)\right)+\delta\left(x\right)\right)=0. \tag{10}$$

- **Step 2:** Using Shehu transform characteristics[29] to the Eq. (10) with the initial condition, it gives:

$$\mathbb{S}\left(y\left(x\right)\right)=\left(\frac{s_2}{s_1}\right)^{m}\sum_{r=0}^{m-1}\left(\frac{s_2}{s_1}\right)^{m-r-1}y^{(r)}\left(0\right)-\left(\frac{s_2}{s_1}\right)^{m}\mathbb{S}\left(R\left(y\left(x\right)\right)+N\left(y\left(x\right)\right)+\delta\left(x\right)\right). \tag{11}$$

- **Step 3:** Applying the inverse Shehu transform to the Eq. (11) yields:

$$y\left(x\right)=\mathcal{R}\left(x\right)-\mathbb{S}^{-1}\left[\left(\frac{s_2}{s_1}\right)^{m}\mathbb{S}\left(R\left(y\left(x\right)\right)+N\left(y\left(x\right)\right)\right)\right], \tag{12}$$

where $\mathcal{R}(x)$ denotes an expression obtained from the original term and implementation of initial conditions.

- **Step 4:** Subsequently, via reduced differential transform, Eq. (12) is expressed as:

$$Y\left(0\right)=\mathcal{R}\left(x\right). \tag{13}$$

$$Y\left(i+1\right)=-\mathbb{S}^{-1}\left[\left(\frac{s_2}{s_1}\right)^{m}\mathbb{S}\left(R\left(y\left(x\right)\right)+N\left(y\left(x\right)\right)\right)\right], \tag{14}$$

where $R(Y(i))$ and $N(Y(i))$ are transformations for $R(y(x))$ and $N(y(x))$, respectively.

- **Step 5:** The analytical approximate solution to the Eq. (9) is expressed as a series of infinite terms that gradually converge to an accurate solution, as demonstrated below:

$$y\left(x\right)=\sum_{i=0}^{\infty}Y\left(i\right). \tag{15}$$

- **Step 6:** Padé approximant of order $[n,\ d]$ is applied to a series derived in (15). Although the values of n and d are selected at random, they are restricted to being less than the order of the power series. This approach extends the solution's domain, improving its convergence and accuracy.

Formulating governing equations

This research investigates semi-analytical solutions for three-dimensional magnetohydrodynamic flow of a Casson tri-hybrid nanofluid ($TiO_2 - SiO_2 - Al_2O_3$) over a bidirectionally stretched surface. The fluid flows along x- and y-axes, with z-axis perpendicular to the flow direction. The surface stretching velocities are defined as $u_w = \hat{c}x$ and $v_w = \hat{b}x$, where $\hat{c}$ and $\hat{b}$ are positive constants. A magnetic field of strength M_0 is applied along z-axis, perpendicular to x- and y-axes. The parameter $\widehat{h}_f$ denotes the heat transfer coefficient at the heated surface. The temperatures T_∞, T_w, and T_f represent free-stream, surface, and fluid temperatures, respectively, satisfying the condition $T_\infty < T_w < T_f$. Fig. 1 illustrates the physical configuration of the system.

Based on these assumptions, governing equations are formulated as follows:[39,40]

$$\frac{\partial u}{\partial x}+\frac{\partial v}{\partial y}+\frac{\partial w}{\partial z}=0, \tag{16}$$

$$u\frac{\partial u}{\partial x}+v\frac{\partial u}{\partial y}+w\frac{\partial u}{\partial z}=\frac{\mu_3}{\rho_3}\left(1+\frac{1}{\hat{\beta}}\right)\frac{\partial^2 u}{\partial z^2}-\left(\frac{\sigma_3 {M_0}^2}{\rho_3}+\frac{\mu_3}{\rho_3\mathcal{K}_p}\right)u, \tag{17}$$

$$u\frac{\partial v}{\partial x}+v\frac{\partial v}{\partial y}+w\frac{\partial v}{\partial z}=\frac{\mu_3}{\rho_3}\left(1+\frac{1}{\hat{\beta}}\right)\frac{\partial^2 v}{\partial z^2}-\left(\frac{\sigma_3 {M_0}^2}{\rho_3}+\frac{\mu_3}{\rho_3\mathcal{K}_p}\right)v, \tag{18}$$

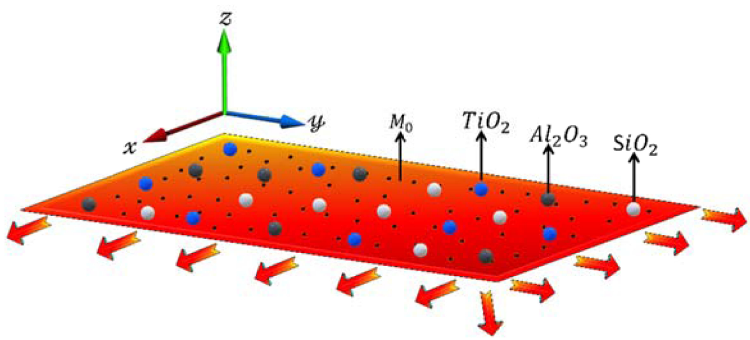

Fig. 1. Schematic of MHD Casson Tri-hybrid nanofluid flow geometry.

$$u\frac{\partial T}{\partial x} + v\frac{\partial T}{\partial y} + w\frac{\partial T}{\partial z} = \frac{1}{(\rho C_p)_3}\left(\left(k_3 + \frac{16\,\hat{\sigma}\,T_\infty^3}{3\hat{k}}\right)\frac{\partial^2 T}{\partial z^2} + q_1\,(T - T_\infty) + \hat{q}_2\,(T_f - T_\infty)\,e^{-\hat{a}\hat{\eta}}\right). \tag{19}$$

with boundary conditions:

$$\begin{gathered} u = u_w + \mathcal{A}\tfrac{\partial u}{\partial z},\ v = v_w + \mathcal{B}\tfrac{\partial v}{\partial z}, \\ w = 0,\ -k_3\tfrac{\partial T}{\partial z} = \hat{h}_f\,(T_f - T)\ \text{at}\ z = 0, \\ u, v \to 0,\ T \to T_\infty\ \text{as}\ z \to \infty. \end{gathered} \tag{20}$$

where $\mathcal{A}$ and $\mathcal{B}$ denote slip constants, $\mathcal{K}_p$ represents the permeability of a porous medium, $\hat{\beta}$ is Casson parameter, $\hat{\sigma}$ is Stefan-Boltzmann constant, and q_1 and q_2 are coefficients of thermal-dependent and space-dependent heat source parameters, respectively. k_3 indicates thermal conductivity, μ_3 is dynamic viscosity, ρ_3 is density, σ_3 represents electrical conductivity, and $(\rho C_p)_3$ refers to the heat capacity of tri-hybrid nanofluid ($TiO_2 - SiO_2 - Al_2O_3$) combined with blood, as defined in [41]:

$$\frac{k_1}{k_0} = \frac{k_{TiO_2} + 2k_0 - 2\emptyset_{TiO_2}\,(k_0 - k_{TiO_2})}{k_{TiO_2} + 2k_0 + \emptyset_{TiO_2}\,(k_0 - k_{TiO_2})},$$

$$\frac{k_2}{k_1} = \frac{k_{SiO_2} + 2k_1 - 2\emptyset_{SiO_2}\,(k_1 - k_{SiO_2})}{k_{SiO_2} + 2k_1 + \emptyset_{SiO_2}\,(k_1 - k_{SiO_2})},$$

$$\frac{k_3}{k_2} = \frac{k_{Al_2O_3} + 2k_2 - 2\emptyset_{Al_2O_3}\,(k_2 - k_{Al_2O_3})}{k_{Al_2O_3} + 2k_2 + \emptyset_{Al_2O_3}\,(k_2 - k_{Al_2O_3})},$$

$$\mu_3 = \frac{\mu_0}{(1 - \emptyset_{TiO_2})^{2.5}(1 - \emptyset_{SiO_2})^{2.5}(1 - \emptyset_{Al_2O_3})^{2.5}},$$

$$(\rho C_p)_3 = (1 - \emptyset_{TiO_2})\left((1 - \emptyset_{SiO_2})\left((1 - \emptyset_{Al_2O_3})\,(\rho C_p)_0 + \emptyset_{Al_2O_3}(\rho C_p)_{Al_2O_3}\right) + \emptyset_{SiO_2}(\rho C_p)_{SiO_2}\right) + \emptyset_{TiO_2}(\rho C_p)_{TiO_2},$$

$$\rho_3 = (1 - \emptyset_{TiO_2})\,((1 - \emptyset_{SiO_2})\,((1 - \emptyset_{Al_2O_3})\,\rho_0 + \emptyset_{Al_2O_3}\rho_{Al_2O_3}) + \emptyset_{SiO_2}\rho_{SiO_2}) + \emptyset_{TiO_2}\rho_{TiO_2},$$

$$\frac{\sigma_1}{\sigma_0} = \frac{(1 + 2\emptyset_{TiO_2})\,\sigma_{TiO_2} + 2\,(1 - \emptyset_{TiO_2})\,\sigma_0}{(1 - \emptyset_{TiO_2})\,\sigma_{TiO_2} + (2 + \emptyset_{TiO_2})\,\sigma_0},$$

Table 1. Calculated values of TiO_2, SiO_2, Al_2O_3, and blood.[40,42,43]

Material properties	TiO_2	SiO_2	Al_2O_3	Blood
$k(W/m\,K)$	8.9538	1.4013	40	0.492
$\rho(Kg/m^3)$	4250	2200	3970	1063
$C_p(J/Kg\,K)$	686.2	754	765	3594
$\sigma(S/m)$	$2.4*10^6$	$3.5*10^6$	$36.9*10^6$	0.8

$$\frac{\sigma_2}{\sigma_1}=\frac{\left(1+2\emptyset_{SiO_2}\right)\sigma_{SiO_2}+2\left(1-\emptyset_{SiO_2}\right)\sigma_1}{\left(1-\emptyset_{SiO_2}\right)\sigma_{SiO_2}+\left(2+\emptyset_{SiO_2}\right)\sigma_1},$$

$$\frac{\sigma_3}{\sigma_2}=\frac{(1+2\emptyset_{Al_2O_3})\sigma_{Al_2O_3}+2(1-\emptyset_{Al_2O_3})\sigma_2}{(1-\emptyset_{Al_2O_3})\sigma_{Al_2O_3}+(2+\emptyset_{Al_2O_3})\sigma_2}.$$

Table 1 presents measured values of tri-hybrid nanofluid and blood. The similarity transformations[40]:

$$\begin{gathered}u=\hat{c}xf(\hat{\eta}),\; v=\hat{c}y g(\hat{\eta}),\; w=-\sqrt{\hat{c}\nu_0}\left(f(\hat{\eta})+g(\hat{\eta})\right),\\ T=T_\infty+\left(T_f-T_\infty\right)\vartheta(\hat{\eta}),\; \hat{\eta}=z\sqrt{\tfrac{\hat{c}}{\nu_0}}.\end{gathered}\tag{21}$$

By applying the above substitutions to simplify Eqs. (16) to (19) into ordinary differential equations, we obtain:

$$\left(1+\frac{1}{\beta}\right)f'''(\hat{\eta})-\Pi_1\Pi_2\left(f'^2(\hat{\eta})-\left(f(\hat{\eta})+g(\hat{\eta})\right)f''(\hat{\eta})\right)-\left(\Pi_1\Pi_3\hat{\mathrm{M}}+\mathcal{K}\right)f'(\hat{\eta})=0,\tag{22}$$

$$\left(1+\frac{1}{\beta}\right)g'''(\hat{\eta})-\Pi_1\Pi_2\left(g'^2(\hat{\eta})-\left(f(\hat{\eta})+g(\hat{\eta})\right)g''(\hat{\eta})\right)-\left(\Pi_1\Pi_3\hat{\mathrm{M}}+\mathcal{K}\right)g'(\hat{\eta})=0,\tag{23}$$

$$(\Pi_4+\mathcal{R}d)\vartheta''(\hat{\eta})+\Pi_S\mathcal{P}r\left(f(\hat{\eta})+g(\hat{\eta})\right)\vartheta'(\hat{\eta})+\mathcal{P}r\Pi_T\vartheta(\hat{\eta})+\mathcal{P}r\Pi_S e^{-\hat{a}\hat{\eta}}=0,\tag{24}$$

Given boundary conditions:

$$\begin{gathered}f(0)=0,\quad g(0)=0,\quad f'(0)=1+\alpha f''(0),\\ g'(0)=\beta_1+\hat{\Upsilon}g''(0),\quad -\Pi_4\vartheta'(0)=\mathcal{B}i\left(\vartheta(0)-1\right),\\ f',\quad g',\quad \vartheta\to 0\quad \text{as } \hat{\eta}\to\infty.\end{gathered}\tag{25}$$

Dimensionless parameters are outlined as follows:

$$\Pi_1=\frac{\mu_0}{\mu_3},\; \Pi_2=\frac{\rho_3}{\rho_0},\; \Pi_3=\frac{\sigma_3}{\sigma_0},\; \Pi_4=\frac{k_3}{k_0},\; \Pi_5=\frac{(\rho C_p)_3}{(\rho C_p)_0},$$

$$\mathcal{P}r=\frac{(\rho C_p)_0}{k_0},\; \mathcal{R}d=\frac{16\hat{\sigma}T_\infty^3}{3\hat{k}k_0},\; \beta_1=\frac{\hat{b}}{\hat{c}},$$

$$\Pi_T=\frac{q_1}{\hat{c}(\rho C_p)_0},\; \Pi_S=\frac{q_2}{\hat{c}(\rho C_p)_0},\; \mathcal{B}i=\frac{\widehat{\hbar}_f}{k_0}\sqrt{\frac{\nu_0}{\hat{c}}},$$

$$\alpha=\mathcal{A}\sqrt{\frac{\hat{c}}{\nu_0}},\mathcal{K}=\frac{\mu_0}{\hat{c}\rho_0\mathcal{K}_p},\; \hat{\mathrm{M}}=\frac{\sigma_0 M_0^2}{\hat{c}\rho_0},\; \hat{\Upsilon}=\mathcal{B}\sqrt{\frac{\hat{c}}{\nu_0}},$$

where $\mathcal{B}i$ represents the Biot number, β_1 denotes stretching ratio parameter, ν_0 indicates the kinematic viscosity of blood, $\mathcal{K}$ signifies porosity parameter, and α and $\hat{\Upsilon}$ are slip parameters along x- and y-axes, respectively.

The formulas for shear stresses, $\hat{\tau}_{wx}$ and $\hat{\tau}_{wy}$, along x- and y-axes, respectively, as well as heat flux, $\widehat{q}_w$, can be derived as follows:

$$\hat{\tau}_{wx} = \mu_3 \left.\frac{\partial u}{\partial z}\right|_{z=0},\ \hat{\tau}_{wy} = \mu_3 \left.\frac{\partial v}{\partial z}\right|_{z=0},\ \widehat{q}_w = -\left(k_3 + \frac{16\,\hat{\sigma}\,T_\infty^3}{3\hat{k}}\right)\left.\frac{\partial T}{\partial z}\right|_{z=0}. \tag{26}$$

The skin friction coefficient, $\hat{C}_{fx}$ and $\hat{C}_{fx}$, corresponding to x- and y-axes, respectively, along with the Nusselt number, Nu_x, are physical quantities and are given as follows:

$$\hat{C}_{fx} = \frac{\hat{\tau}_{wx}}{0.5\,\rho\,u_w^2},\ \hat{C}_{fy} = \frac{\hat{\tau}_{wy}}{0.5\,\rho\,u_w^2}, \mathcal{N}u_x = \frac{x\,\widehat{q}_w}{k_0\left(T_f - T_\infty\right)}. \tag{27}$$

By applying a similarity transformation, Eq. (27) is transformed as follows:

$$\hat{C}_{fx}\mathcal{R}e_x^{0.5} = \frac{1}{\Pi_1}f''(0),\ \hat{C}_{fy}\mathcal{R}e_y^{0.5} = \frac{1}{\Pi_1}g''(\hat{\eta}),\ \mathcal{N}u_x\mathcal{R}e_x^{-0.5} = -\Pi_4\left(1+\mathcal{R}d\right)\vartheta'(0), \tag{28}$$

where $\mathcal{R}e_x$ is the Reynolds number.

Implementation SRDTPM

In this section, the SRDTPM method is applied to solve Eqs. (22) to (24) and obtain analytical approximate solutions for heat transfer in the flow of a tri-hybrid nanofluid ($TiO_2 - SiO_2 - Al_2O_3$) of Casson type. The flow is influenced by magnetohydrodynamic (MHD) forces over a stretched surface in a bidirectional porous medium. The main steps of this method are presented:

- **Step 1:** Applying Shehu transform to Eqs. (22) to (24) results in the following:

$$\mathbb{S}\left(f(\hat{\eta})\right) = \Lambda_1(0) + \frac{\beta}{\beta+1}\left(\frac{s_2}{s_1}\right)^3 \mathbb{S}\begin{pmatrix}\Pi_1\Pi_2\left(f'^2(\hat{\eta}) - \left(f(\hat{\eta}) + g(\hat{\eta})\right)f''(\hat{\eta})\right)\\ +\left(\Pi_1\Pi_3\hat{\mathrm{M}} + \mathcal{K}\right)f'(\hat{\eta})\end{pmatrix}, \tag{29}$$

$$\mathbb{S}\left(g(\hat{\eta})\right) = \Lambda_2(0) + \frac{\beta}{\beta+1}\left(\frac{s_2}{s_1}\right)^3 \mathbb{S}\begin{pmatrix}\Pi_1\Pi_2\left(g'^2(\hat{\eta}) - \left(f(\hat{\eta}) + g(\hat{\eta})\right)g''(\hat{\eta})\right)\\ \left(\Pi_1\Pi_3\hat{\mathrm{M}} + \mathcal{K}\right)g'(\hat{\eta})\end{pmatrix}, \tag{30}$$

$$\mathbb{S}\left(\vartheta(\hat{\eta})\right) = \frac{s_2}{s_1}\vartheta(0) + \left(\frac{s_2}{s_1}\right)^2\vartheta'(0) - \frac{1}{\Pi_4 + \mathcal{R}d}\left(\frac{s_2}{s_1}\right)^2 \mathbb{S}\begin{pmatrix}\Pi_5\,\mathcal{P}r\,\left(f(\hat{\eta}) + g(\hat{\eta})\right)\vartheta'(\hat{\eta})\\ \mathcal{P}r\,\Pi_T\,\vartheta(\hat{\eta}) + \mathcal{P}r\,\Pi_S\,e^{-\hat{a}\hat{\eta}}\end{pmatrix}, \tag{31}$$

where $\Lambda_1(0) = \frac{s_2}{s_1}f(0) + (\frac{s_2}{s_1})^2 f'(0) + (\frac{s_2}{s_1})^3 f''(0)$, $\Lambda_2(0) = \frac{s_2}{s_1}g(0) + (\frac{s_2}{s_1})^2 g'(0) + (\frac{s_2}{s_1})^3 g''(0)$

- **Step 2:** Using initial conditions $f(0) = g(0) = 0$, $f'(0) = 1 + \alpha f''(0)$, $g'(0) = \beta_1 + \hat{\Upsilon}\ g''(0)$, and $-\Pi_4\vartheta'(0) = \mathcal{B}i\ (\vartheta(0) - 1)$, while assuming $f''(0) = \hat{c}_1$, $g''(0) = \hat{c}_2$, and $\vartheta(0) = \hat{c}_3$, the inverse Shehu transform is applied to Eqs. (29) to (31) to obtain final results:

$$f(\hat{\eta}) = (1 + \alpha\hat{c}_1)\hat{\eta} + \frac{\hat{c}_1}{2}\hat{\eta}^2 + \Lambda\mathbb{S}^{-1}\left[\left(\frac{s_2}{s_1}\right)^3 \mathbb{S}\begin{pmatrix}\Pi_1\Pi_2\left(f'^2(\hat{\eta}) - \left(f(\hat{\eta}) + g(\hat{\eta})\right)f''(\hat{\eta})\right)\\ +\left(\Pi_1\Pi_3\hat{\mathrm{M}} + \mathcal{K}\right)f'(\hat{\eta})\end{pmatrix}\right], \tag{32}$$

$$g(\hat{\eta}) = \left(\beta_1 + \hat{\Upsilon}\hat{c}_2\right)\hat{\eta} + \frac{\hat{c}_2}{2}\hat{\eta}^2 + \Lambda\mathbb{S}^{-1}\left[\left(\frac{s_2}{s_1}\right)^3 \mathbb{S}\begin{pmatrix}\Pi_1\Pi_2\left(g'^2(\hat{\eta}) - \left(f(\hat{\eta}) + g(\hat{\eta})\right)g''(\hat{\eta})\right)\\ \left(\Pi_1\Pi_3\hat{\mathrm{M}} + \mathcal{K}\right)g'(\hat{\eta})\end{pmatrix}\right], \tag{33}$$

$$\vartheta(\hat{\eta}) = \hat{c}_3 + \frac{\mathcal{B}i}{\Pi_4}(1-\hat{c}_3)\hat{\eta} - \frac{1}{\Pi_4+\mathcal{R}d}\mathbb{S}^{-1}\left[\left(\frac{s_2}{s_1}\right)^2 \mathbb{S}\left(\begin{array}{c}\Pi_5\,\mathcal{P}r\,\left(f(\hat{\eta})+g(\hat{\eta})\right)\vartheta'(\hat{\eta})\\ \mathcal{P}r\,\Pi_T\,\vartheta(\hat{\eta})+\mathcal{P}r\,\Pi_S e^{-\hat{a}\hat{\eta}}\end{array}\right)\right], \quad (34)$$

where $\Lambda = \frac{\beta}{\beta+1}$

- **Step 3:** Then, using the reduced differential transform, Eqs. (32) to (34) become:

$$F(i+3) = \Lambda\mathbb{S}^{-1}\left[\left(\frac{s_2}{s_1}\right)^3 \mathbb{S}\left(\Pi_1\Pi_2\left(\Delta_1(i)-\Delta_2(i)\right)+\left(\Pi_1\Pi_3\hat{\mathrm{M}}+\mathcal{P}r\right)(i+1)F(i+1)\right)\right], \quad (35)$$

$$\mathcal{G}(i+3) = \Lambda\ \mathbb{S}^{-1}\left[\left(\frac{s_2}{s_1}\right)^3 \mathbb{S}\left(\Pi_1\Pi_2\left(\Delta_3(i)-\Delta_4(i)\right)+\left(\Pi_1\Pi_3\hat{\mathrm{M}}+\mathcal{K}\right)(i+1)\mathcal{G}(i+1)\right)\right], \quad (36)$$

$$\Theta(i+2) = -\frac{1}{\Pi_4+\mathcal{R}d}\mathbb{S}^{-1}\left[\left(\frac{s_2}{s_1}\right)^2 \mathbb{S}\left(\Pi_5\,\mathcal{P}r\,\Delta_5(i)+\mathcal{P}r\,\Pi_T\Theta(i)+\mathcal{P}r\,\Pi_S\frac{(-\hat{a})^i}{i!}\right)\right]. \quad (37)$$

with

$$\begin{array}{l} F(0)=0,\ F(1)=(1+\hat{\alpha}\hat{c}_1)\hat{\eta},\ F(2)=\frac{\hat{c}_1}{2}\hat{\eta}^2,\\ \mathcal{G}(0)=0,\ \mathcal{G}(1)=\left(\beta_1+\hat{\Upsilon}\hat{c}_2\right)\hat{\eta},\ \mathcal{G}(2)=\frac{\hat{c}_2}{2}\hat{\eta}^2,\\ \quad\Theta(0)=\hat{c}_3,\ \Theta(1)=\frac{\mathcal{B}i}{\Pi_4}(1-\hat{c}_3)\hat{\eta}, \end{array} \quad (38)$$

where $\Delta_1(i)$, $\Delta_2(i)$, $\Delta_3(i)$, $\Delta_4(i)$, and $\Delta_5(i)$ represent reduced differential transforms of terms $f'^2(\hat{\eta})$, $(f(\hat{\eta})+g(\hat{\eta}))f''(\hat{\eta})$, $g'^2(\hat{\eta})$, $(f(\hat{\eta})+g(\hat{\eta}))g''(\hat{\eta})$, and $(f(\hat{\eta})+g(\hat{\eta}))\vartheta'(\hat{\eta})$ respectively. These terms take form:

$$\Delta_1(i) = \sum_{j=0}^{i}(i-j+1)(j+1)F(j+1)F(i-j+1),$$

$$\Delta_2(i) = \sum_{j=0}^{i}(i-j+1)(i-j+2)\left(F(j)+\mathcal{G}(j)\right)F(i-j+2),$$

$$\Delta_3(i) = \sum_{j=0}^{i}(i-j+1)(j+1)\mathcal{G}(j+1)\mathcal{G}(i-j+1),$$

$$\Delta_4(i) = \sum_{j=0}^{i}(i-j+1)(i-j+2)\left(F(j)+\mathcal{G}(j)\right)\mathcal{G}(i-j+2),$$

$$\Delta_5(i) = \sum_{j=0}^{i}(i-j+1)(F(j)+\mathcal{G}(j))\Theta(i-j+1).$$

From Eqs. (35) to (37), and 38 we get:

$$F(0) = 0, \quad (39)$$

$$F(1) = (1+\hat{\alpha}\hat{c}_1)\hat{\eta}, \quad (40)$$

$$F(2) = \frac{\hat{c}_1}{2}\hat{\eta}^2, \quad (41)$$

$$F(3) = \Lambda\left(\hat{c}_1\hat{\alpha}+1\right)\left[\frac{1}{24}\left(\Pi_1\Pi_3\hat{\mathrm{M}}+\mathcal{K}\right)\hat{\eta}^4+\frac{1}{60}\Pi_1\Pi_2\left(\hat{c}_1\alpha+1\right)\ \hat{\eta}^5\right], \tag{42}$$

$$F(4) = \frac{\Lambda\hat{c}_1}{60}\left(\Pi_1\Pi_3\hat{\mathrm{M}}+\mathcal{K}\right)\ \hat{\eta}^5-\frac{\Pi_1\Pi_2\ \Lambda\hat{c}_1}{120}\left(\hat{\beta}_1+\hat{c}_2\hat{\Upsilon}-\hat{c}_1\alpha-1\right)\ \hat{\eta}^6, \tag{43}$$

$$\mathcal{G}(0) = 0, \tag{44}$$

$$\mathcal{G}(1) = \left(\beta_1+\hat{\Upsilon}\hat{c}_2\right)\hat{\eta}, \tag{45}$$

$$\mathcal{G}(2) = \frac{\hat{c}_2}{2}\hat{\eta}^2, \tag{46}$$

$$\mathcal{G}(3) = \Lambda\left(\hat{c}_2\hat{\Upsilon}+\beta_1\right)\left[\frac{1}{24}\left(\Pi_1\Pi_3\hat{\mathrm{M}}+\mathcal{K}\right)\hat{\eta}^4+\frac{\Pi_1\Pi_2}{60}\left(\hat{c}_2\hat{\Upsilon}+\beta_1\right)\ \hat{\eta}^5\right], \tag{47}$$

$$\mathcal{G}(4) = \frac{\Lambda\hat{c}_2}{60}\left(\Pi_1\Pi_3\hat{\mathrm{M}}+\mathcal{K}\right)\hat{\eta}^5+\frac{\Pi_1\Pi_2\ \Lambda\hat{c}_1}{120}\left(\beta_1+\hat{c}_2\hat{\Upsilon}-\hat{c}_1\alpha-1\right)\ \hat{\eta}^6, \tag{48}$$

$$\Theta(0) = \hat{c}_3, \tag{49}$$

$$\Theta(1) = \frac{\mathcal{B}i}{\Pi_4}\left(1-\hat{c}_3\right)\hat{\eta}, \tag{50}$$

$$\Theta(2) = -\frac{\mathcal{P}r\left(\hat{c}_3\Pi_T+\Pi_S\right)}{2\left(\Pi_4+\mathcal{R}d\right)}\hat{\eta}^2, \tag{51}$$

$$\Theta(3) = \frac{\mathcal{P}r}{2\left(\Pi_4+\mathcal{R}d\right)}\left[\hat{a}\Pi_S\hat{\eta}^2+\frac{\mathcal{B}i\ \Pi_T\left(\hat{c}_3-1\right)}{3\Pi_4}\hat{\eta}^3+\frac{\mathcal{B}i\ \Pi_5\left(\hat{c}_3-1\right)\left(\beta_1+\hat{c}_2\hat{\Upsilon}+\hat{c}_1\alpha+1\right)}{6\Pi_4}\hat{\eta}^4\right], \tag{52}$$

solutions derived from SRDTPM are detailed below:

$$f(\hat{\eta}) = \sum_{i=0}^{4} F(i), \tag{53}$$

$$g(\hat{\eta}) = \sum_{i=0}^{4} \mathcal{G}(i), \tag{54}$$

$$\vartheta(\hat{\eta}) = \sum_{i=0}^{3} \Theta(i). \tag{55}$$

Finally, Padé approximant of order $[0,5]$ was computed for $f'(\hat{\eta})$ and $g'(\hat{\eta})$, whereas Padé approximant of order $[0,4]$ was calculated for $\vartheta(\hat{\eta})$. The boundary conditions outlined in Eq. (25) were employed to find constants $\hat{c}_1$, $\hat{c}_2$, and $\hat{c}_3$.

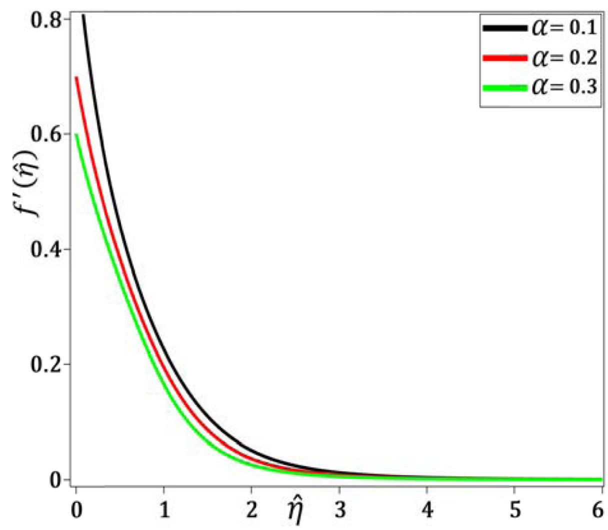

Fig. 2. $\hat{\alpha}$ impact on $f'(\hat{\eta})$.

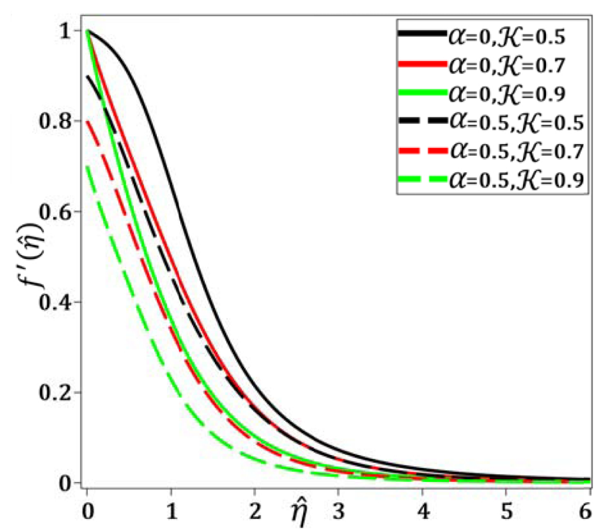

Fig. 3. Porosity influence on $f'(\hat{\eta})$.

Results and discussion

This section examines the solutions obtained by SRDTPM to analyze heat transfer in the flow of a Casson-type tri-hybrid nanofluid ($TiO_2 - SiO_2 - Al_2O_3$). The flow is affected by magnetohydrodynamic forces over a bidirectionally stretched porous surface, with emphasis on convective heating, using blood as the base fluid. The findings are corroborated by comparison with previous investigations.[40] The study investigates the influence of key parameters, including thermal radiation, spatial and temporal heat sources in the energy equations, and magnetic forces in the momentum equations. The fixed parameter values are: $\hat{\mathrm{M}} = 1, \mathcal{K} = 1,\ \beta = 0.5, \mathcal{Bi} = 3, \mathcal{Pr} = 21, \Pi_T = \Pi_S = 2, \mathcal{Rd} = 1,\ \emptyset_{TiO_2} = \emptyset_{SiO_2} = \emptyset_{Al_2O_3} = 0.02$. Fig. 2 illustrates the influence of the slip parameter (α) on primary velocity curves of tri-hybrid nanofluid, $f'(\hat{\eta})$, along x-axis. As (α) rises, the velocity curve decreases. This occurs because the interaction between the fluid and the stretching surface decreases with a higher (α), leading to greater fluid slip and reduced friction. The reduced friction enhances heat transfer efficiency, and in medical applications, it improves blood flow in devices that involve sliding motion, thereby lowering the risk of blood clotting.

Fig. 3 depicts the influence of the porosity parameter ($\mathcal{K}$) on $f'(\hat{\eta})$ curves. The velocity curve decreases as ($\mathcal{K}$) increases, with (α) fixed at 0 and 0.5. This occurs because larger void spaces in the porous medium at

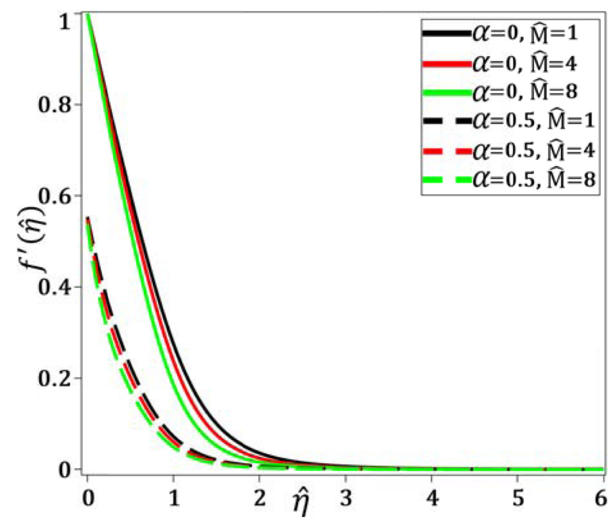

Fig. 4. Magnetic impact on $f'(\hat{\eta})$.

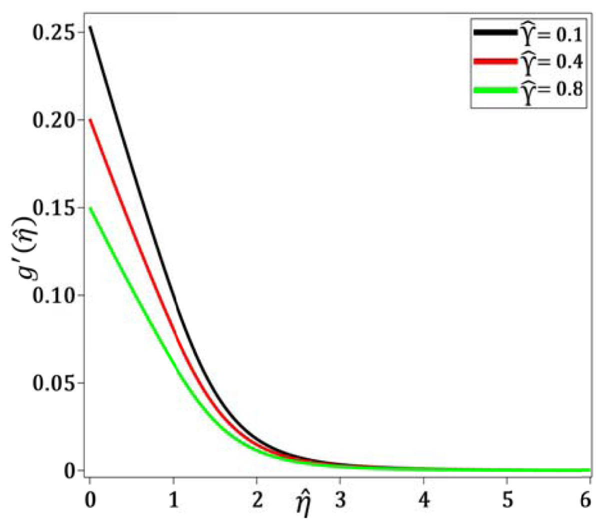

Fig. 5. $\hat{\Upsilon}$ impact on $g'(\hat{\eta})$.

higher ($\mathcal{K}$) hinder fluid flow and reduce velocity. Medically, permanent porosity in blood vessels increases resistance to blood flow, as observed in conditions such as arteriosclerosis. Fig. 4 illustrates the impact of the magnetic field intensity parameter ($\hat{\mathrm{M}}$) on $f'(\hat{\eta})$ curves. As ($\hat{\mathrm{M}}$) increases, $f'(\hat{\eta})$ curves decrease for fluid flow over the stretching surface at both $\alpha = 0$ and $\alpha = 0.5$. This is due to the stronger Lorentz force generated by an increased magnetic field, which resists fluid motion and reduces velocity. The reduction in velocity is more pronounced when slip is present, particularly at $\alpha = 0.5$. Medically, in cases such as controlling bleeding, the reduction in blood flow speed caused by a stronger magnetic field can help lower pressure within blood vessels.

Fig. 5 represents the effect of slip parameter ($\hat{\Upsilon}$) on secondary velocity curves $g'(\hat{\eta})$ along y-axis. As ($\hat{\Upsilon}$) increases, secondary velocity curves decrease, indicating greater slip of the fluid on the stretching surface in the vertical direction. A higher ($\hat{\Upsilon}$) enhances fluid slip, thereby reducing lateral momentum. Medically, a reduction in velocity due to increased ($\hat{\Upsilon}$) may affect the distribution of medications in specific regions of blood vessels. Fig. 6 presents the relationship between porosity parameter ($\mathcal{K}$) and secondary velocity $g'(\hat{\eta})$. The secondary velocity curves decrease as ($\mathcal{K}$) increases, while ($\hat{\Upsilon}$) remains constant at 0 and 0.5. The expansion of voids within the porous structure, especially at $\hat{\Upsilon} = 0.5$, leads to improved fluid movement. In terms of biomedical engineering, the effect of porous media and slip effects on blood flow velocity will reduce its velocity, thus facilitating better diffusion and even distribution of drugs. In Fig. 7, the effect of the varying ($\hat{\mathrm{M}}$) on the value of

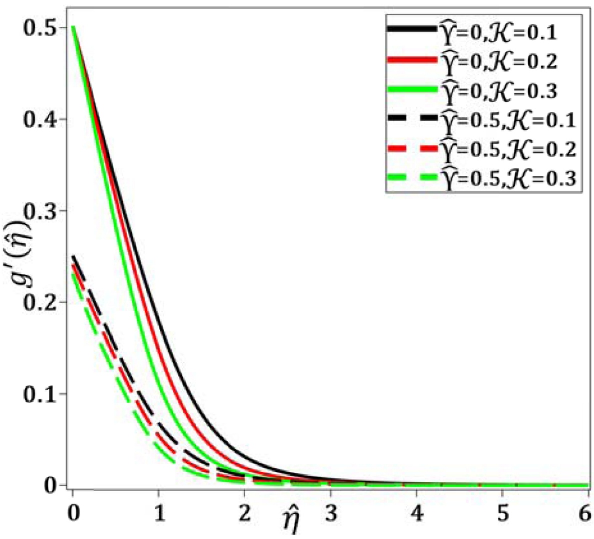

Fig. 6. Porosity influence on $g'(\hat{\eta})$.

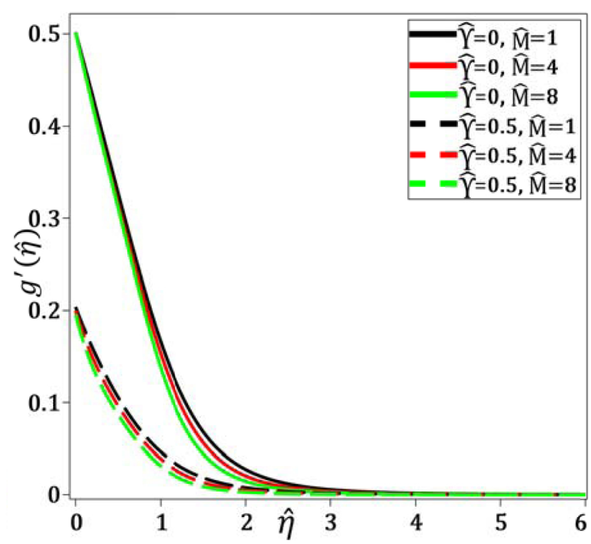

Fig. 7. Magnetic impact on $g'(\hat{\eta})$.

$g'(\hat{\eta})$ has been illustrated. The increase in ($\hat{M}$) is causing the reduction in $g'(\hat{\eta})$ for the flow above the stretching surface, and this is regardless of whether $\hat{\Upsilon}$is equal to 0 or equal to 0.5. This behavior is also attributed to the enhanced Lorentz force that is generated by the higher value of ($\hat{M}$), which also acting to the resist fluid motion and the diminish velocity. From a medical point of view, integrating the slip phenomena with the effects of magnetic fields enables the regulation of fluid velocity and may be used to enhance blood circulation or delivery of pharmaceuticals in the body. Fig. 8 shows how the Casson parameter (β) is affecting the profiles of $g'(\hat{\eta})$ for the slip parameters $\hat{\Upsilon} = 0$ and $\hat{\Upsilon} = 0.5$. With increasing values of (β), it can be observed that there is improvement in secondary velocity due to surface stretching in both slip cases. Physically speaking, increased value of (β) implies higher magnitude of shear stress necessary to initiate motion, resulting in higher $g'(\hat{\eta})$ along y-axis. In a medical view, the higher value of (β) could facilitate improved drug transport in the blood vessels because of more effective interaction between the circulating medication and the blood flow. Fig. 9 shows the impact of the radiation parameter ($\mathcal{R}d$) on the temperature distributions $\vartheta(\hat{\eta})$. From results, it is observed that high values of ($\mathcal{R}d$) result in a marked increase in the value of $\vartheta(\hat{\eta})$. ($\mathcal{R}d$) is an indication of radiative heat transfer occurring in the system. As the value of ($\mathcal{R}d$) increases, radiative heat transfer takes place in higher volumes and, therefore, increases the total heat transfer rate within the liquid. Physically,

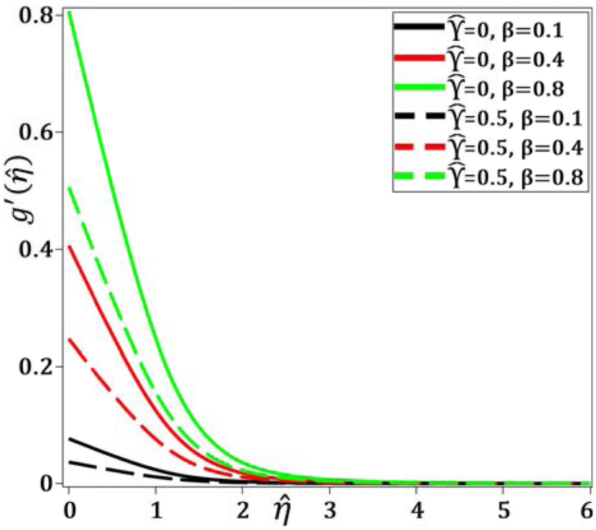

Fig. 8. $\hat{\beta}$ impact on $g'(\hat{\eta})$.

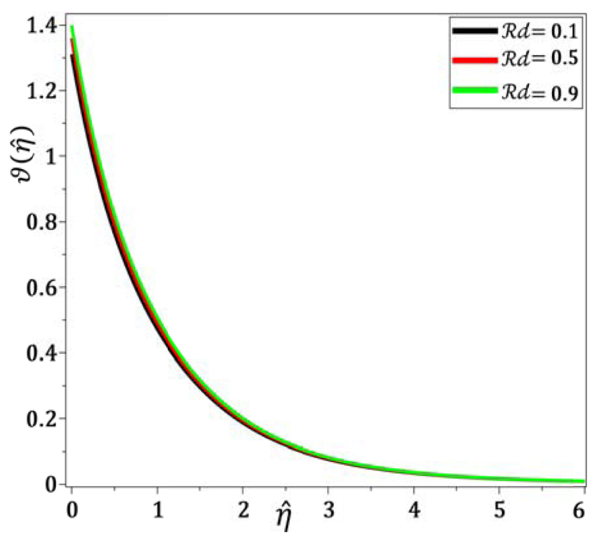

Fig. 9. $\widehat{\mathcal{R}d}$ impact on $\tilde{\vartheta}(\hat{\eta})$.

this means that radiative heat transfer becomes more efficient than conductive and convective heat transfer. From a medical perspective, an increased $(\mathcal{R}d)$ aids in even distribution of heat through the bloodstream, and this helps protect the body fluids from any thermal hazards. Fig. 10 analyses the effect of the heat source parameter with temperature dependence (Π_T) on $\vartheta(\hat{\eta})$ behavior with respect to radiation parameter values of 0 and 0.5. An observable trend is observed in both instances where there is an increase in the $\vartheta(\hat{\eta})$ for heat flow across a bidirectional stretching surface. Physically speaking, increasing (Π_T) or $(\mathcal{R}d)$ increases thermal effectiveness, hence an increase in $\vartheta(\hat{\eta})$ in the surface region. Fig. 11 illustrates the influence of the position-dependent heat source parameter (Π_S) on $\vartheta(\hat{\eta})$ at constant values of $(\mathcal{R}d)$. With an increase in (Π_S), the profiles of $\vartheta(\hat{\eta})$ experience considerable enhancements under the two circumstances. Higher (Π_S) facilitates the creation of larger amounts of internal heat within the fluid. Additionally, the role played by $(\mathcal{R}d)$ leads to more uniform distribution of the heat, thereby enhancing $\vartheta(\hat{\eta})$. In the medical field, the relationship between (Π_S) and $(\mathcal{R}d)$ contributes significantly toward reducing thermal stresses in bodily fluids and tissues. Fig. 12 highlights the influence of changes in Biot number $(\mathcal{B}i)$ on the $\vartheta(\hat{\eta})$ graphs at values 0 and 0.5 of the radiation parameter $(\mathcal{R}d)$. The increase in $(\mathcal{B}i)$ in both cases greatly influences $\vartheta(\hat{\eta})$ graphs during fluid flow in a stretchable surface. In terms of physical significance, high values of $(\mathcal{B}i)$ and $(\mathcal{R}d)$ promote better transfer of thermal energy, enabling wider heat distribution in the fluid and over the surface. Biologically speaking, such

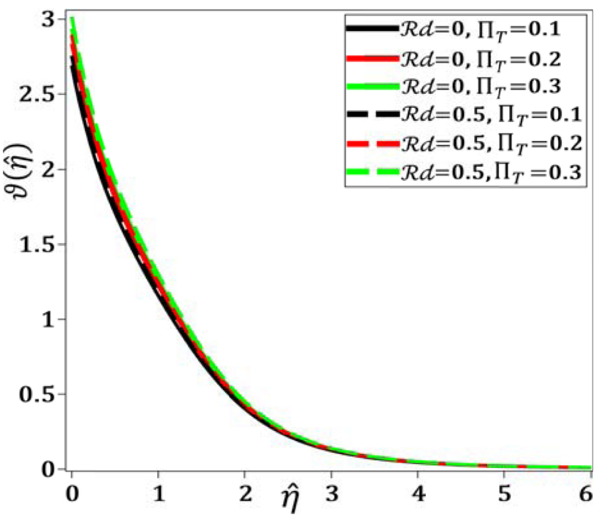

Fig. 10. Π_T influence on $\vartheta(\hat{\eta})$.

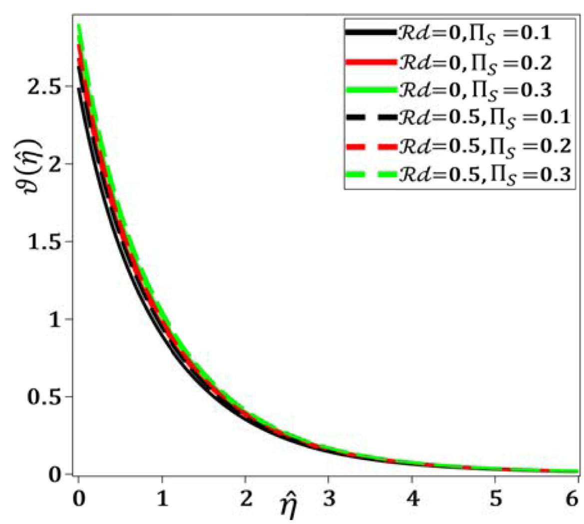

Fig. 11. Π_S influence on $\vartheta(\hat{\eta})$.

an effect by these two parameters will ensure more uniform heat distribution in tissues to a certain area of interest. Fig. 13 and Fig. 14 are showing the behavior of the permeability parameter ($\mathcal{K}$) on the skin friction ($\hat{C}_{fx}\mathcal{R}e_x^{0.5}$)and $\hat{C}_{fy}\mathcal{R}e_y^{0.5}$) on the x-axis for $\alpha = 0$ up to $\alpha = 0.5$, and on the y-axis for $\hat{\Upsilon} = 0$ up to $\hat{\Upsilon} = 0.5$. The results are showing that the augmenting both the permeability and the magnetic parameters ($\hat{\mathrm{M}}$) is resulting in the elevated skin friction values with both axes under the specified α and $\hat{\Upsilon}$ conditions. This effect is arising because of the intensified fluid motion and the stronger interaction between the fluid and the porous surface at higher magnetic field strengths. From a biomedical view, such an increase would play an important role in enhancing the blood flow within tissues and promoting key physiological activities. Fig. 15 is showing how the parameter (Π_S) can affect the Nusselt number ($\mathcal{N}u_x\mathcal{R}e_x^{-0.5}$) for ($\mathcal{R}d$) values set at 0 up to 0.5. The data demonstrate that as (Π_S) and (Π_T) increase, there can be a corresponding rise in the value of ($\mathcal{N}u_x\mathcal{R}e_x^{-0.5}$), with the effect being more pronounced when the value of $\mathcal{R}d = 0.5$.

Physically, an increase in ($\mathcal{N}u_x\mathcal{R}e_x^{-0.5}$) means better heat transfer through the fluid, which improves the thermal distribution on surfaces that are stretched two-way. Medically, such an improvement helps in dilating blood vessels and increasing blood flow to certain areas. Fig. 16 shows the effect of changing the value of the permeability parameter ($\mathcal{K}$) on fluid dynamics through the graphs below ($\mathcal{K} = 0.1$, $\mathcal{K} = 0.2$, and $\mathcal{K} = 0.3$). At $\mathcal{K} = 0.1$, the effect of low porosity in the medium causes considerable restrictions on the fluid motion.

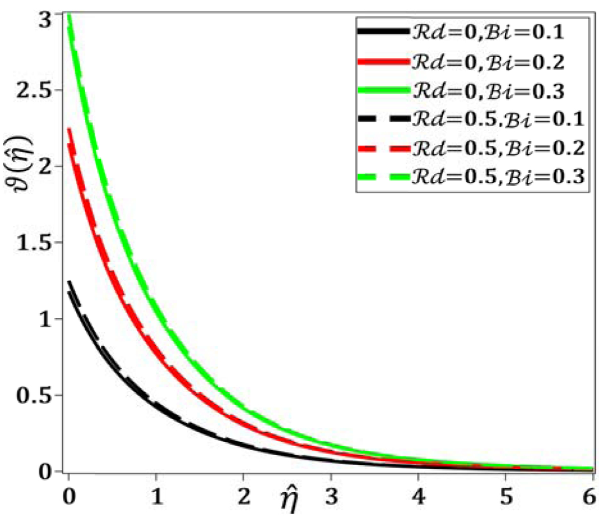

Fig. 12. $\mathcal{B}i$ impact on $\vartheta(\hat{\eta})$.

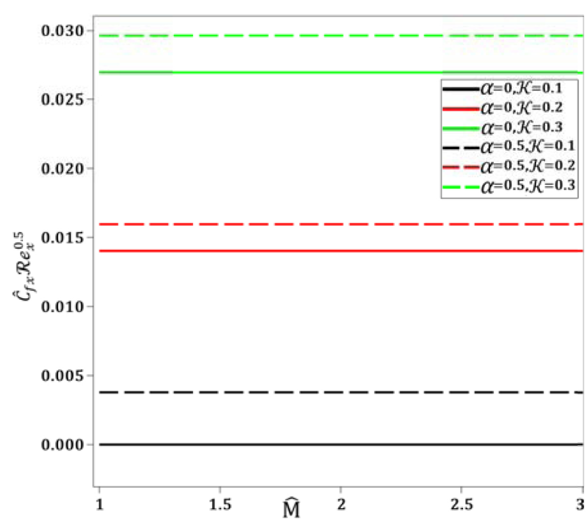

Fig. 13. Coupled effect of $\mathcal{K}$ and $\hat{\mathrm{M}}$ on $\hat{C}_{fx}\mathcal{R}e_x^{0.5}$.

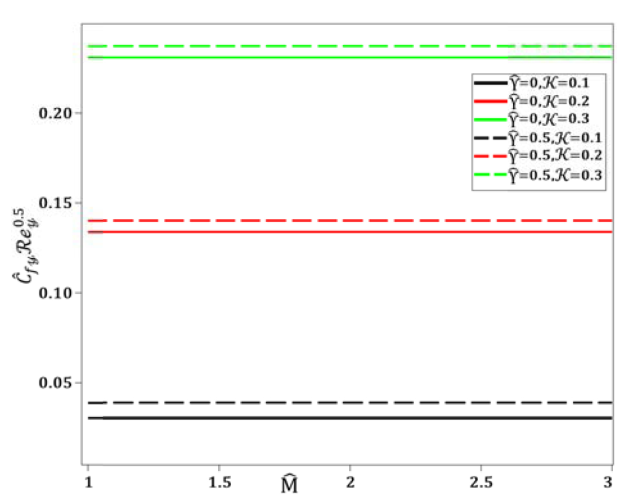

Fig. 14. Combined effect of $\mathcal{K}$ and $\hat{\mathrm{M}}$ on $\hat{C}_{fy}\mathcal{R}e_y^{0.5}$.

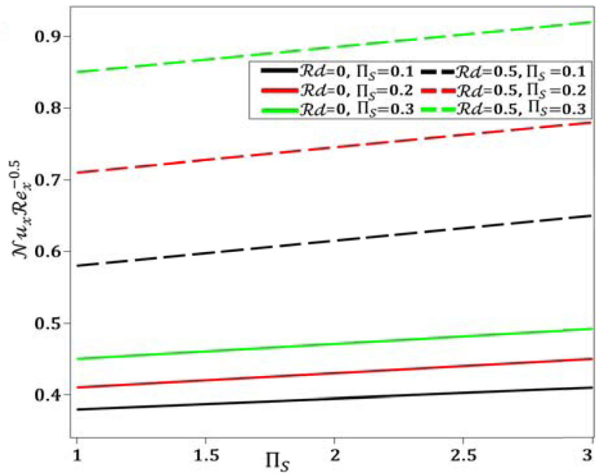

Fig. 15. Combined effect of Π_S and Π_T on $\mathcal{N}u_x\mathcal{R}e_x^{-0.5}$.

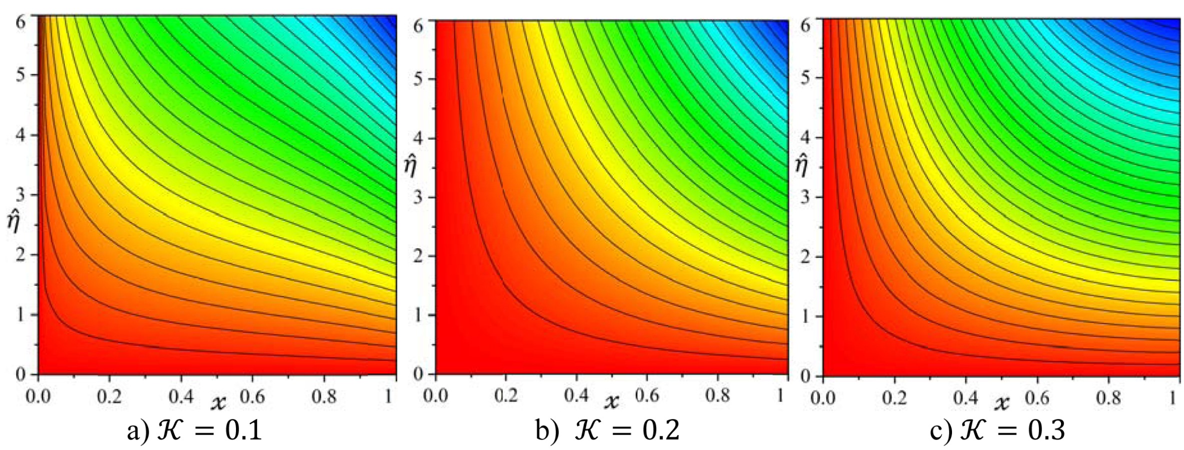

Fig. 16. Contour plot showing effect of different values of $\mathcal{K}$ on blood flow.

Table 2. Skin friction coefficients $(\hat{C}_{fx}\mathcal{R}e_x^{0.5})$ and $(\hat{C}_{fy}\mathcal{R}e_y^{0.5})$: SRDTPM, Runge-Kutta-Fehlberg method (RKFM), and homotopy analysis method (HAM).

	SRDTPM		RKFM[39]		HAM[40]	
α	$\hat{C}_{fx}\mathcal{R}e_x^{0.5}$	$\hat{C}_{fy}\mathcal{R}e_y^{0.5}$	$\hat{C}_{fx}\mathcal{R}e_x^{0.5}$	$\hat{C}_{fy}\mathcal{R}e_y^{0.5}$	$\hat{C}_{fx}\mathcal{R}e_x^{0.5}$	$\hat{C}_{fy}\mathcal{R}e_y^{0.5}$
0	1	0	1	0	1	0
0.1	1.020262	0.066849	1.020260	0.066847	1.020260	0.066847
0.2	1.039496	0.148738	1.039495	0.148737	1.039495	0.148737
0.3	1.057956	0.243361	1.057955	0.243360	1.057955	0.243360
0.4	1.075790	0.349211	1.075788	0.349209	1.075788	0.349209
0.5	1.093097	0.465208	1.093095	0.465205	1.093095	0.465205
0.6	1.109947	0.590532	1.109944	0.590529	1.109944	0.590529
0.7	1.126399	0.724533	1.126398	0.724532	1.126398	0.724532
0.8	1.142491	0.866685	1.142489	0.866683	1.142489	0.866683
0.9	1.158255	1.016540	1.158254	1.016539	1.158254	1.016539
1	1.173723	1.173722	1.173721	1.173721	1.173721	1.173721

At $\hat{\mathcal{K}} = 0.2$, the effect of higher pore volume on permeability causes ease of flow. For $\mathcal{K} = 0.3$.The effect of the medium is small enough that it allows the easy flow of fluids. Table 2 and Table 3 compare the results from the current work with those in the literature[39,40] and[44,45], respectively. Table 2 addresses the skin friction coefficient $(\hat{C}_{fx}\mathcal{R}e_x^{0.5})$ across different values of (α), whereas Table 3 lists $(\hat{C}_{fy}\mathcal{R}e_y^{0.5})$ as $(\hat{\mathrm{M}})$ varies,

Table 3. Skin friction coefficients ($\hat{C}_{fx}\mathcal{R}e_x^{0.5}$): SRDTPM, RKFM, HAM, and variational iteration method (VIM).

$\hat{M}$	SRDTPM	RKFM [39]	HAM [40]	VIM [44]	RKFM [45]
0	1.000009	1.000008	1.000008	1.000008	—
1	1.414217	1.414214	1.414214	1.414214	1.41421
5	2.449494	2.449490	2.449490	2.449490	2.4494
10	3.316625	3.316625	3.316625	3.316625	3.3166
50	7.141429	7.141428	7.141428	7.141428	7.1414
100	10.049878	10.049875	10.04987	10.049876	10.0498
500	22.383030	22.383029	22.38302	22.383029	22.38302
1000	31.638587	31.638584	31.63858	31.638584	—

Table 4. Skin friction ($\hat{C}_{fx}\mathcal{R}e_x^{0.5}$) analysis along x-axis: SRDTPM and HAM.

		SRDTPM		HAM [40]	
$\hat{M}$	$\mathcal{K}$	α=0	$\alpha = 0.5$	α=0	$\alpha = 0.5$
0.1		0.457949	0.507955	0.457942	0.507953
0.2		0.467588	0.527646	0.467587	0.527644
0.3		0.486750	0.546434	0.486747	0.546432
0.4		0.508735	0.560745	0.508733	0.560743
	0.1	0.797539	0.853264	0.797536	0.853263
	0.2	0.805376	0.873153	0.805374	0.873152
	0.3	0.814675	0.895338	0.814673	0.895336
	0.4	0.823466	0.912355	0.823464	0.912353

Table 5. Analysis of skin friction ($\hat{C}_{fy}\mathcal{R}e_y^{0.5}$) along y-axis: SRDTPM and homotopy analysis method (HAM).

		SRDTPM		HAM [40]	
$\hat{M}$	$\mathcal{K}$	$\hat{\Upsilon} = 0$	$\hat{\Upsilon} = 0.5$	$\hat{\Upsilon} = 0$	$\hat{\Upsilon} = 0.5$
0.1		0.686449	0.721458	0.686447	0.721454
0.2		0.697647	0.743255	0.697643	0.743253
0.3		0.705218	0.764255	0.705215	0.764253
0.4		0.72046	0.781215	0.720456	0.781214
	0.1	0.552667	0.624537	0.552663	0.624535
	0.2	0.567998	0.632248	0.567994	0.632246
	0.3	0.57423	0.646789	0.574225	0.646784
	0.4	0.580241	0.657877	0.580235	0.657874

and having all other variables kept as constant. The comparison shows a high degree of consistency between the current findings and the previously published work, thereby validating the precision and reliability of the adopted method. Table 4 and Table 5 further elaborate on the effects of ($\hat{M}$) and ($\mathcal{K}$) on ($\hat{C}_{fx}\mathcal{R}e_x^{0.5}$) for ($\alpha = 0$) and ($\alpha = 0.5$), as well as on ($\hat{C}_{fy}\mathcal{R}e_y^{0.5}$) for ($\hat{\Upsilon} = 0$) and ($\hat{\Upsilon} = 0.5$). The findings consistently show that both ($\hat{C}_{fx}\mathcal{R}e_x^{0.5}$) and ($\hat{C}_{fy}\mathcal{R}e_y^{0.5}$) increase as ($\hat{M}$) and ($\mathcal{K}$) rise, underscoring the direct influence of these parameters on skin friction coefficients.

Table 6 analyzes the effect of parameters (Π_S), (Π_T), and ($\mathcal{B}i$) on Nusselt number ($\mathcal{N}u_x\mathcal{R}e_x^{-0.5}$) at ($\mathcal{R}d = 0$) and ($\mathcal{R}d = 0.5$). The findings indicate a clear increase in the Nusselt number as (Π_S), (Π_T), and ($\mathcal{B}i$) rise, with most significant change observed when ($\mathcal{R}d = 0.5$). Table 7 presents a comparison between SRDTPM and RDTM by measuring errors and CPU time for primary and secondary velocity and temperature, using ($L_2 = \sqrt{\hat{h}\sum_{i=0}^{\mathcal{N}} |\hat{\varepsilon}_{i+1}(\hat{\eta}) - \hat{\varepsilon}_i(\hat{\eta})|^2}$, $L_\infty = \max_{i=0\ldots\mathcal{N}} |\hat{\varepsilon}_{i+1}(\hat{\eta}) - \hat{\varepsilon}_i(\hat{\eta})|$). This table demonstrates that the new approach provides superior accuracy and efficiency relative to RDTM, since it produces improved outcomes with smaller errors and lower CPU time for both primary and secondary velocity and temperature.

Table 6. Nusselt number ($\mathcal{N}u_x \mathcal{R}e_x^{-0.5}$) analysis: SRDTPM and homotopy analysis method (HAM).

			SRDTPM		HAM [40]	
Π_S	Π_T	$\mathcal{B}i$	$\mathcal{R}d$=0	$\mathcal{R}d = 0.5$	$\mathcal{R}d = 0$	$\mathcal{R}d = 0.5$
0.1			0.686448	0.721456	0.686447	0.721454
0.2			0.697645	0.743255	0.697643	0.743253
0.3			0.705217	0.764255	0.705215	0.764253
0.4			0.720457	0.781216	0.720456	0.781214
	0.1		0.552665	0.624538	0.552663	0.624535
	0.2		0.567995	0.632249	0.567994	0.632246
	0.3		0.574226	0.646787	0.574225	0.646784
	0.4		0.580236	0.657877	0.580235	0.657874
		0.1	0.865438	0.885486	0.865436	0.885484
		0.2	0.896435	0.915745	0.896432	0.915743
		0.3	0.925429	0.942125	0.925426	0.942123
		0.4	0.954265	0.972158	0.954263	0.972156

Table 7. Errors and CPU time for SRDTPM and RDTM.

Functions	Errors	SRDTPM	RDTM
Primary velocity $f'(\hat{\eta})$	L_2	0.01359	0.04076
	L_∞	0.03989	0.11967
	CPU(s)	0.047	0.109
Secondary velocity $g'(\hat{\eta})$	L_2	0.02011	0.05165
	L_∞	0.04883	0.12981
	CPU(s)	0.049	0.114
Temperature $\vartheta(\hat{\eta})$	L_2	0.03522	0.04579
	L_∞	0.05387	0.16579
	CPU(s)	0.047	0.11

Convergence analysis of SRDTPM

This section analyzes essential conditions for the convergence of analytical approximate solutions obtained in Eqs. (53) to (55) utilizing SRDTPM.

Definition: Let $\tilde{\Gamma} : \hat{\chi} \to \mathbb{R}$ represent a nonlinear operator, where $\hat{\chi}$ is a Banach space and $\mathbb{R}$ is set of real numbers. The sequence of approximations is expressed as:

$$\hat{\Psi}_{\kappa+1} = \tilde{\Gamma}\left(\hat{\Psi}_\kappa\right), \ \hat{\Psi}_\kappa = \sum_{\omega=0}^{\kappa} \psi_\omega, \ \omega = 0, 1, 2, \ldots$$

If $\tilde{\Gamma}$ satisfies the Lipschitz condition with a constant $\sigma \in \mathbb{R}$, inequality holds:

$\|\tilde{\Gamma}(\hat{\Psi}_\kappa) - \tilde{\Gamma}(\hat{\Psi}_{\kappa-1})\| \le \sigma \|\hat{\Psi}_\kappa - \hat{\Psi}_{\kappa-1}\|, \ 0 < \sigma < 1.$

Theorem: The series solution $\hat{\psi} = \sum_{\omega=0}^{\infty} \psi_\omega$, derived using SRDTPM, converges if the following condition is satisfied:

$\|\hat{\Psi}_{\kappa+1} - \hat{\Psi}_\kappa\| \to 0$ as $\kappa \to \infty, \ 0 < \sigma < 1.$

Proof:

$$\|\hat{\Psi}_{\kappa+1} - \hat{\Psi}_\kappa\| = \|\sum_{\omega=0}^{\kappa+1} \psi_\omega - \sum_{\omega=0}^{\kappa} \psi_\omega\| = \|\sum_{\omega=0}^{\kappa+1} \mathbb{S}_1^{-1}\left[\hat{\mathcal{F}}_\omega\right] - \sum_{\omega=0}^{\kappa} \mathbb{S}_1^{-1}\left[\hat{\mathcal{F}}_\omega\right]\|$$

$$= \|\mathbb{S}_1^{-1} \sum_{\omega=0}^{\kappa+1} \left[\hat{\mathcal{F}}_\omega\right] - \mathbb{S}_1^{-1} \sum_{\omega=0}^{\kappa} \left[\hat{\mathcal{F}}_\omega\right]\|$$

Using $\hat{\Psi}_{\kappa+1} = \tilde{\Gamma}(\hat{\Psi}_\kappa)$, we get:

$$\|\hat{\Psi}_{\kappa+1} - \hat{\Psi}_\kappa\| = \|\mathbb{S}_1^{-1}\tilde{\Gamma} \sum_{\omega=0}^{\kappa} \left[\hat{\mathcal{F}}_\omega\right] - \mathbb{S}_1^{-1}\tilde{\Gamma} \sum_{\omega=0}^{\kappa-1} \left[\hat{\mathcal{F}}_\omega\right]\| = \|\mathbb{S}_1^{-1}\tilde{\Gamma}\left[\sum_{\omega=0}^{\kappa} \psi_\omega\right] - \mathbb{S}_1^{-1}\tilde{\Gamma}\left[\sum_{\omega=0}^{\kappa-1} \psi_\omega\right]\|$$

Table 8. Power comparison of σ^{κ} for $f'(\hat{\eta})$, $g'(\hat{\eta})$ and $\vartheta(\hat{\eta})$ in SRDTPM and RDTM.

Function	Method	σ^0	σ^1	σ^2	...
Primary velocity $\tilde{f}'(\hat{\eta})$	SRDTPM	0.27665	0.01344	0.00341	...
	RDTM	0.41498	0.02017	0.00847	...
Secondary velocity $g'(\hat{\eta})$	SRDTPM	0.22021	0.01204	0.00775	...
	RDTM	0.44043	0.02409	0.01989	...
Temperature $\vartheta(\hat{\eta})$	SRDTPM	0.79265	0.56321	0.33701	...
	RDTM	0.95118	0.79285	0.66827	...

$$\leq \left|\mathbb{S}_1^{-1}\right| \|\tilde{\Gamma}\left[\sum_{\omega=0}^{\kappa}\psi_{\omega}\right] - \tilde{\Gamma}\left[\sum_{\omega=0}^{\kappa-1}\psi_{\omega}\right]\| \leq \sigma\|\mathbb{S}_1^{-1}\sum_{\omega=0}^{\kappa}[\hat{\mathcal{F}}_{\omega}] - \mathbb{S}_1^{-1}\sum_{\omega=0}^{\kappa-1}[\hat{\mathcal{F}}_{\omega}]\|$$

$$\leq \sigma^2\|\mathbb{S}_1^{-1}\sum_{\omega=0}^{\kappa-1}[\hat{\mathcal{F}}_{\omega}] - \mathbb{S}_1^{-1}\sum_{\omega=0}^{\kappa-2}[\hat{\mathcal{F}}_{\omega}]\|$$

$$\leq \sigma^{\kappa}\|\mathbb{S}_1^{-1}\sum_{\omega=0}^{1}[\hat{\mathcal{F}}_{\omega}] - \mathbb{S}_1^{-1}\sum_{\omega=0}^{0}[\hat{\mathcal{F}}_{\omega}]\|$$

$$= \sigma^{\kappa}\|\hat{\Psi}_1 - \hat{\Psi}_0\| \to 0 \text{ as } \kappa \to \infty,\ 0 < \sigma < 1,\ \mathbb{S}_1^{-1}(.) = (\frac{\widehat{q}}{\widehat{p}})^3\mathbb{S}(.).$$

From this theorem, we can find the values of the parameters σ^{κ} to achieve convergence using following definition:

$$\sigma^{\kappa} = \begin{cases} \frac{\|\hat{\Psi}_{\kappa+1}-\hat{\Psi}_{\kappa}\|}{\|\hat{\Psi}_1-\hat{\Psi}_0\|}, & \hat{\Psi}_1 \neq \hat{\Psi}_0, \kappa = 1, 2, \ldots, \\ 0 & \hat{\Psi}_1 = \hat{\Psi}_0, \end{cases}$$

Now, we can obtain convergence of the problem using the relation above. Furthermore, the convergence results of analytical approximate solutions obtained through two methods, SRDTPM and RDTM, are compared and presented in Table 8.

From Table 8, we observe that $\sigma^{\kappa} \to 0$ as $\kappa \to \infty$, for $0 < \sigma < 1$. Additionally, differences in convergence are evident between SRDTPM and RDTM. powers σ obtained using SRDTPM approach zero faster than those obtained using RDTM. Therefore, we conclude that SRDTPM exhibits better convergence compared to RDTM.

Conclusion

In this study, we applied a hybrid analytical approach, Shehu reduced differential transform Padé method (SRDTPM) to derive new approximate solutions for a model describing the magnetohydrodynamic flow of a Casson tri-hybrid nanofluid ($TiO_2 - SiO_2 - Al_2O_3$) over a bidirectionally stretched surface. The model incorporates the influence of hydrodynamic magnetic forces on a stretched surface in a bidirectional porous medium. We examined the effects of various physical parameters, including the slip parameter (α and $\hat{\Upsilon}$), porosity parameter ($\mathcal{K}$), magnetic field intensity parameter ($\hat{\mathrm{M}}$), and Casson parameter (β) on the momentum equation. Additionally, we investigated the impact of the radiation parameter ($\mathcal{R}d$), temperature-dependent heat source parameter (Π_{T}), location-dependent heat source parameter (Π_{S}), and Biot number ($\mathcal{B}i$) on the energy equation. The results, presented in tables and graphs, validate the efficiency of this approach by comparing with previously published findings and demonstrating excellent agreement. The key findings include:

- 1- $f'(\hat{\eta})$ and $g'(\hat{\eta})$ decrease with increasing values of (α) and ($\hat{\Upsilon}$), respectively.
- 2- $f'(\hat{\eta})$ and $g'(\hat{\eta})$ decrease as ($\mathcal{K}$) and ($\hat{\mathrm{M}}$) increase, with a more significant decrease when ($\alpha = 0.5$) and ($\hat{\Upsilon} = 0.5$).
- 3- $\vartheta(\hat{\eta})$ increases with increasing (β) at ($\hat{\Upsilon} = 0,\ 0.5$), with a stronger increase at ($\hat{\Upsilon} =\ 0.5$).
- 4- $\vartheta(\hat{\eta})$ rises with increasing (Π_{T}), (Π_{S}), and ($\mathcal{B}i$) for ($\mathcal{R}d = 0,\ 0.5$).

Nomenclature.

(u, v, w)	Velocity vector components
(x, y, z)	Coordinates axes
α	Slip parameters along x-axis
$\hat{\Upsilon}$	Slip parameters along y-axis
$\hat{\sigma}$	Stefan-Boltzmann constant
T_w	Surface temperature
$\mathcal{K}_p$	Permeability of porous medium
$\mathcal{N}u_x\mathcal{R}e_x^{-0.5}$	Nusselt number
$\hat{\eta}$	Similarity variable
$\mathcal{A}$ and $\mathcal{B}$	Slip constants
T_∞	Free-stream temperature
q_1	Coefficients of thermal-dependent heat source
β_1	Stretching ratio
$\mathcal{B}i$	Biot number
Π_S	Location-dependent heat source parameter
Π_T	Heat source parameter
$\mathcal{R}d$	Radiation parameter
$\mathbb{S}^{-1}$	Inverse Shehu transform
$\hat{\mathrm{M}}$	Magnetic field
ρ	Fluid density
$\mathcal{P}r$	Prandtl number
$\mathcal{K}$	Porosity
ν_0	Kinematic viscosity of blood
T_f	Fluid temperature
q_2	Coefficients of space-dependent heat source
$\hat{\beta}$	Casson factor

- 5- As $(\mathcal{K})$ increases, $(\hat{C}_{fx}\mathcal{R}e_x^{0.5})$ along x-axis and $(\hat{C}_{fy}\mathcal{R}e_y^{0.5})$ along y-axis both increase, with the most significant rise occurring when $(\alpha = 0.5)$ and $(\hat{\Upsilon} = 0.5)$.
- 6- $(\mathcal{N}u_x\mathcal{R}e_x^{-0.5})$ increases with Π_S when $\mathcal{R}d = 0, 0.5$, showing a stronger increase when $\mathcal{R}d = 0.5$.
- 7- Contour plots illustrate that increasing $(\mathcal{K})$ enhances fluid dynamics, effectively reducing resistance within the medium and resulting in a more defined flow.
- 8- The tri-hybrid nanofluid $(TiO_2 - SiO_2 - Al_2O_3)$ significantly enhances heat transfer within a porous medium under the influence of a magnetic field, while also improving fluid flow over a stretched surface.
- 9- Error and convergence analysis demonstrate that SRDTPM achieves lower error, reduced CPU time, and faster convergence than RDTM, confirming its superior performance.

Overall, the results demonstrate the accuracy and efficiency of SRDTPM method, making it a suitable solution for problems involving flow over stretched surfaces or within porous media.

Authors' declaration

- Conflicts of Interest: None.
- We hereby confirm that all the Figures and Tables in the manuscript are ours. Furthermore, any Figures and images that are not ours have been included with the necessary permission for republication, which is attached to the manuscript.
- No animal studies are present in the manuscript.
- No human studies are present in the manuscript.
- Ethical Clearance: The project was approved by the local ethical committee at the University of Basrah.

Authors' contributions statement

The author designed a methodology and performed formal analysis, investigation, and software development. A A wrote the original draft. A J A supervised the study and contributed to reviewing and editing the manuscript. All authors reviewed and approved the final version of the paper.

Data availability

Datasets generated and analyzed during the current study are available from the corresponding author on reasonable request.

References

1. Nasresfahani F, Eslahchi MR. Error analysis of finite difference/collocation method for the nonlinear coupled parabolic free boundary problem modeling plaque growth in artery. Appl Math Comput. 2021 Sep;405:126221. http://dx.doi.org/10.1016/j.amc.2021.126221.
2. Manchi R, Ponalagusamy R. Modeling of pulsatile EMHD flow of Au-blood in an inclined porous tapered atherosclerotic vessel under periodic body acceleration. Arch Appl Mech. 2021 May 11;91(7):3421–47. http://dx.doi.org/10.1007/s00419-021-01974-6.
3. Ali A, Khatoon R, Ashraf M, Awais M. Cattaneo-Christov heat flux on MHD flow of hybrid nanofluid across stretched cylinder with radiations and Joule heating effects. Waves in Random and Complex Media. 2022 Nov 15;1–18. http://dx.doi.org/10.1080/17455030.2022.2145524.
4. Abdel Hameed Asfour H, Ibrahim MG. Numerical simulations and shear stress behavioral for electro-osmotic blood flow of magneto Sutterby nanofluid with modified Darcy's law. Therm Sci Eng Prog. 2023 Jan;37:101599. http://dx.doi.org/10.1016/j.tsep.2022.101599.
5. Bataineh AS, Isik OR, Hashim I. Bernstein collocation method for solving MHD Jeffery-Hamel blood flow problem with error estimations. Int J Differ Equ. 2022 May 11;2022:1–9. http://dx.doi.org/10.1155/2022/9123178.
6. Jamil DF, Uddin S, Kazi M, Roslan R, Gorji MR, Kamalrulzaman Md Akhir M. MHD blood flow effects of Casson fluid with Caputo-Fabrizio fractional derivatives through an inclined blood vessels with thermal radiation. Heliyon. 2023 Nov;9(11):e21780. http://dx.doi.org/10.1016/j.heliyon.2023.e21780.
7. Shamshuddin MD, Saeed A, Kenneth Asogwa K, Usman, Jamshed W. A semi-analytical approach to investigate the entropy generation in a tangent hyperbolic magnetized hybrid nanofluid flow upon a stretchable rotating disk. J Magn Magn Mater. 2023 May;574:170664. http://dx.doi.org/10.1016/j.jmmm.2023.170664.
8. Mangamma Ch, Pramod Kumar P, Malga BS, Appidi L, Matta S. Effect of Dufour and chemical reaction on an unsteady magneto hydrodynamics flow past an exponentially moving plate. Heat Trans. 2024 Jan 16;53(4):1689–1708. http://dx.doi.org/10.1002/htj.23010.
9. Vaidya H, Prasad KV, Tripathi D, Choudhari R, Hanumantha, Ahmad H. Viscoplastic hybrid nanofluids flow through vertical stenosed artery. Bionanoscience. 2023 Oct 24;13(4):2348–2370. http://dx.doi.org/10.1007/s12668-023-01213-y.
10. Gunisetty R, Reddy PBA, A D. Entropy generation analysis on EMHD non-Newtonian hybrid nanofluid flow over a permeable rotating disk through semi analytical and numerical approaches. Proc Inst Mech Eng E J Process Mech Eng. 2023 Sep 14. http://dx.doi.org/10.1177/09544089231199640.
11. Sajjan K, Vishnuvardhana SV, Mamatha SU, Raju CSK. Entropy and non-Fourier flux on hydro-magnetic flow among nonlinearly radiated porous micro walls filled with blood-based different shaped ternary nanoparticles. Int J Appl Comput Math. 2024 May 30;10(3):120. http://dx.doi.org/10.1007/s40819-024-01751-3.
12. Oyekunle TL, Akolade MT, Agunbiade SA, Adeniran PO: MHD stagnation point flow of nanofluid with buoyancy effect through a porous shrinking sheet. Appl Appl Math. 2024 Jun 1;19(1):1–15.
13. khan D. Application of Laplace and Sumudu transforms to modeling of unsteady rotating MHD flow in a second- grade tetra hybrid nanofluid in a porous medium. Adv Mech Eng. 2024 Oct;16(10):16878132241278513. http://dx.doi.org/10.1177/16878132241278513.
14. Agbaje TM, Baithalu R, Mishra SR, Panda S. Irreversibility processes on squeezing flow analysis of blood- based micropolar hybrid nanofluid through parallel channel: spectral quasilinearisation method. Bionanoscience. 2024 May 3;14(3):3226–40. http://dx.doi.org/10.1007/s12668-024-01417-w.
15. Al-Saif ASJ, Zheng-you Z. Upwind local differential quadrature method for solving coupled viscous flow and heat transfer equations. Appl Math Mech. 2004 Oct;25(10):1130–1138. http://dx.doi.org/10.1007/bf02439865.
16. Gireesha BJ, Sowmya G. Heat transfer analysis of an inclined porous fin using differential transform method. Int J Ambient Energy. 2020 Sept 13;43(1):3189–95. http://dx.doi.org/10.1080/01430750.2020.1818619.
17. Al-Botani ZM, Al-Rozbayani AM. Solving Whitham-Broer-Kaup-Like equations numerically by using hybrid differential transform method and finite differences method. Baghdad Sci J. 2022 Feb 1;19(1):1. http://dx.doi.org/10.21123/bsj.2022.19.1.0064.
18. Abdelmoneim MM, Eldabe NT, Abouzeid MY, Ouaf ME. Electro-osmotic peristaltic flow of non-Newtonian Sutterby TiO_2 nanofluid inside a microchannel through porous medium with modified Darcy's law. Mod Phys Lett B. 2024 Sep 30;38(27):2450239. https://doi.org/10.1142/S0217984924502397.
19. Ahsan M, Lei W, Alwuthaynani M, Ahmad M, Nisar M. A higher-order collocation method based on Haar wavelets for integro-differential equations with two-point integral condition. Physica Scripta. 2023 Dec 8;99(1):015211. https://doi.org/10.1088/1402-4896/ad1089.
20. Sohail M, Ilyas K, Rafique E, Singh A, Jahan S. OHAM analysis on bio-convective flow of partial differential equations of Casson nanofluid under thermal radiation impact past over a stretching sheet. BioNanoScience. 2024 Feb 24;14(2):1572–82. http://dx.doi.org/10.1007/s12668-024-01329-9.
21. Pavithra CG, Gireesha BJ, Keerthi ML. Semi-analytical investigation of heat transfer in a porous convective radiative moving longitudinal fin exposed to magnetic field in presence of a shape-dependent trihybrid nanofluid. Appl Math Mech. 2023 Dec 25;45(1):197–216. http://dx.doi.org/10.1007/s10483-024-3069-6.

22. Arif M, Di Persio L, Kumam P, Watthayu W, Akgül A. Heat transfer analysis of fractional model of couple stress Casson tri-hybrid nanofluid using dissimilar shape nanoparticles in blood with biomedical applications. Sci Rep. 2023 Mar 21;13(1). http://dx.doi.org/10.1038/s41598-022-25127-z.
23. Al-Griffi TAJ, Al-Saif AJ. Modify homotopy perturbation method using yang transform to study effect of magnetic field with mass and heat transfer on pulsatile blood flow in tapered stenosis arteries. Heat Trans. 2022 Dec 8;52(3):2249–76. http://dx.doi.org/10.1002/htj.22783.
24. Al-Griffi TAJ, Ali Al-Saif ASJ. An approach for computational blood flow under joint effects of electro- osmotic, magnetic field, chemical reaction and porosity. Eng Comput. 2023 Oct 12;40(7/8):1851–1888. http://dx.doi.org/10.1108/ec-06-2022-0390.
25. Abdulameer YA, Al-Saif AJA. FLT-HPM for two-dimensional transient natural convection in a horizontal cylindrical concentric annulus. Power Eng Thermophy. 2023 May 18;2(3):120–138. http://dx.doi.org/10.56578/peet020301.
26. Ahsan M, Lei W, Bohner M, Khan AA. A high-order multi-resolution wavelet method for nonlinear systems of differential equations. Mathematics and Computers in Simulation. 2024 Jan 1;215:543–59. https://doi.org/10.1016/j.matcom.2023.08.032.
27. Abdul-Wahab MS, Al-Saif ASJA. Studying effects of electro-osmotic and several parameters on blood flow in stenotic arteries using CAGHPM. Partial Differ Equ Appl Math. 2024 Sep;11:100767. http://dx.doi.org/10.1016/j.padiff.2024.100767.
28. Ahsan M, Lei W, Junaid M, Ahmed M, Alwuthaynani M. A numerical solver based on Haar wavelet to find the solution of fifth-order differential equations having simple, two-point and two-point integral conditions. J Appl Math Comput. 2024 Dec;70(6):5575–601. https://doi.org/10.1007/s12190-024-02176-3.
29. Maitama S, Zhao W. New integral transform: Shehu transform a generalization of Sumudu and Laplace transform for solving differential equations. Int J Anal Appl. 2019;17(2):167–190. http://dx.doi.org/10.28924/2291-8639-17-2019-167.
30. Khalouta A, Kadem A. A new modification of reduced differential transform method for nonlinear fractional partial differential equations. J Appl Math Comput Mech. 2020 Sep;19(3):45–58. http://dx.doi.org/10.17512/jamcm.2020.3.04.
31. Chu Y, Bani Hani EH, El-Zahar ER, Ebaid A, Shah NA. Combination of Shehu decomposition and variational iteration transform methods for solving fractional third order dispersive partial differential equations. Numer Methods Partial Differ Equ. 2021 Jan 18;40(2). http://dx.doi.org/10.1002/num.22755.
32. Keskin Y, Oturanç G. Reduced differential transform method for partial differential equations. Int J Nonlinear Sci Numer Simul. 2009 Jun 1;10(6):741–750. http://dx.doi.org/10.1515/ijnsns.2009.10.6.741.
33. Pattnaik PK, Jena S, Mishra S, Mathur P. Application to differential transform method for MHD fluid flow and heat transfer. Biointerface Res Appl Chem. 2022 Mar 24;13(2):110.
34. Liaqat MI, Khan A, Alqudah MA, Abdeljawad T. Adapted homotopy perturbation method with Shehu transform for solving conformable fractional nonlinear partial differential equations. Fractals. 2023 Jan;31(02). https://doi.org/10.1142/S0218348X23400273.
35. Moosavi Noori SR, Taghizadeh N. Study of convergence of reduced differential transform method for different classes of differential equations. Int J Differ Equ. 2021 Apr 30;2021(1):1–16. http://dx.doi.org/10.1155/2021/6696414.
36. Moosavi Noori SR, Taghizadeh N. Modified differential transform method for solving linear and nonlinear pantograph type of differential and Volterra integro-differential equations with proportional delays. Adv Differ Equ. 2020 Nov 19;2020(1). http://dx.doi.org/10.1186/s13662-020-03107-9.
37. Al-Sadi RO, Al-Saif ASJ. Development and simulation of a mathematical model representing dynamics of type 1 diabetes mellitus with treatment. Partial Differ Equ Appl Math. 2023 Dec;8:100575. http://dx.doi.org/10.1016/j.padiff.2023.100575.
38. Akinfe TK, Loyinmi AC. A solitary wave solution to generalized Burgers-Fisher's equation using an improved differential transform method: A hybrid scheme approach. Heliyon. 2021 May;7(5):e07001. http://dx.doi.org/10.1016/j.heliyon.2021.e07001.
39. Yusuf TA, Mabood F, Khan WA, Gbadeyan JA. Irreversibility analysis of Cu-TiO2-H2O hybrid-nanofluid impinging on a 3-D stretching sheet in a porous medium with nonlinear radiation:Darcy-Forchhiemer's model. Alex Eng J. 2020 Dec;59(6):5247–61. http://dx.doi.org/10.1016/j.aej.2020.09.053.
40. Lone SA, Khan A, Raiza Z, Alrabaiah H, Shahab S, Saeed A, *et al.* A semi-analytical solution of the magnetohydrodynamic blood-based ternary hybrid nanofluid flow over a convectively heated bidirectional stretching surface under velocity slip conditions. AIP Adv. 2024 Apr 1;14(4). http://dx.doi.org/10.1063/5.0201663.
41. Shahzadi I, Duraihem FZ, Ijaz S, Raju CSK, Saleem S. Blood stream alternations by mean of electroosmotic forces of fractional ternary nanofluid through oblique stenosed aneurysmal artery with slip conditions. Int J Heat Mass Transf. 2023 Apr;143:106679.http://dx.doi.org/10.1016/j.icheatmasstransfer.2023.106679.
42. Akshatha HD, Sachhin SM, Mahabaleshwar US, Lodhi RK, Ramesh K. Dynamics of Sodium alginate-based ternary nanofluid flow over a stretching sheet with Al2O3, SiO2, and TiO2 nanoparticles. Multiscale Multidiscip Model Exp Des. 2024 Nov 8;8(1). http://dx.doi.org/10.1007/s41939-024-00591-4.
43. Abdulridah SI, Jasim AM. Semi-analytical assessment of magneto-hydrodynamic nano-fluid flow Jeffrey- Hamel problem. Baghdad Sci J. 2024 Jan 1;21(1). http://dx.doi.org/10.21123/bsj.2023.7955.
44. Xu L, Lee EWM. Variational iteration method for magnetohydrodynamic flow over a nonlinear stretching sheet. Abstr Appl Anal. 2013;2013:1–5. http://dx.doi.org/10.1155/2013/573782.
45. Mabood F, Das K. Melting heat transfer on hydromagnetic flow of a nanofluid over a stretching sheet with radiation and second-order slip. Eur Phys J Plus. 2016 Jan;131(1). http://dx.doi.org/10.1140/epjp/i2016-16003-1.

نهج هجين جديد لدراسة التدفق المغناطيسي الهيدروديناميكي للسائل النانوي فوق سطح ممدد

عمار الصالح ، عبدالستار جابر السيف

قسم الرياضيات، كلية التربية للعلوم الصرفة، جامعة البصرة، البصرة، العراق.

الخلاصة

يركز التحقيق الحالي على تطوير تقنية شبه تحليلية تهدف إلى تقدير حلول تدفق الديناميكا المائية المغناطيسية مع سائل نانوي ثلاثي الهجين كاسون (TiO_2-SiO_2-⟦Al⟧_2 O_3/دم) يتدفق فوق سطح قابل للتمدد على طول الفضاء ثنائي الأبعاد. لحل المعادلات التفاضلية غير الخطية المقترحة في صياغة المشكلة، تم استخدام طريقة شبه تحليلية Shehu reduced differential transform Padé method (SRDTPM). تم النظر في عدة معلمات فيزيائية، مثل تأثير الانزلاق، المسامية، القوة المغناطيسية، ورقم كاسون، لفحص التأثير على الزخم، بينما تم تحليل معامل الإشعاع، توليد/ امتصاص الحرارة، مصطلح مصدر/ مستقبل الحرارة المعتمد على درجة الحرارة، ورقم Biot لنقل الطاقة. كشفت النتائج عن علاقة عكسية بين سرعة السائل (كل من السرعات الأولية والثانوية) والتمدد/ القوة المغناطيسية، في حين أن زيادة قيمة رقم كاسون أدت إلى زيادة في السرعة الثانوية. علاوة على ذلك، لوحظ أن القيم الأعلى لمصادر/ مصارف الحرارة وأرقام Biot أدت إلى زيادة في درجة حرارة السائل.

الكلمات المفتاحية: تحليل التقارب، تقريب باديّ، طريقة التحويل التفاضلي المخفض، تحويل شيهو، السائل النانوي الهجين الثلاثي.